

PHYSICAL PROCESSES SHAPING GAMMA-RAY BURST X-RAY AFTERGLOW LIGHT CURVES: THEORETICAL IMPLICATIONS FROM THE *SWIFT* X-RAY TELESCOPE OBSERVATIONS

BING ZHANG,¹ Y. Z. FAN,^{1,2,3} JAROSLAW DYKS,^{1,4} SHIHO KOBAYASHI,^{5,6,7} PETER MÉSZÁROS,^{5,6}
 DAVID N. BURROWS,⁵ JOHN A. NOUSEK,⁵ AND NEIL GEHRELS⁸

Received 2005 August 15; accepted 2005 December 19

ABSTRACT

With the successful launch of the *Swift* Gamma-Ray Burst Explorer, a rich trove of early X-ray afterglow data has been collected by its onboard X-Ray Telescope (XRT). Some interesting features are emerging, including a distinct rapidly decaying component preceding the conventional afterglow component in many sources, a shallow decay component before the more “normal” decay component observed in a good fraction of GRBs, and X-ray flares in nearly half of the afterglows. In this paper we systematically analyze the possible physical processes that shape the properties of the early X-ray afterglow light curves and use the data to constrain various models. We suggest that the steep decay component is consistent with the tail emission of the prompt gamma-ray bursts and/or the X-ray flares. This provides strong evidence that the prompt emission and afterglow emission are likely two distinct components, supporting the internal origin of the GRB prompt emission. The shallow decay segment observed in a group of GRBs suggests that very likely the forward shock keeps being refreshed for some time. This might be caused by either a long-lived central engine, or a wide distribution of the shell Lorentz factors, or else possibly the deceleration of a Poynting flux–dominated flow. X-ray flares suggest that the GRB central engine is very likely still active after the prompt gamma-ray emission is over, but with a reduced activity at later times. In some cases, the central engine activity even extends to days after the burst triggers. Analyses of early X-ray afterglow data reveal that GRBs are indeed highly relativistic events and that early afterglow data of many bursts, starting from the beginning of the XRT observations, are consistent with the afterglow emission from an ISM environment.

Subject headings: gamma rays: bursts — radiation mechanisms: nonthermal — shock waves

1. INTRODUCTION

With the successful launch of the *Swift* Gamma-Ray Burst Explorer, an era of systematic, multiwavelength observations of gamma-ray burst (GRB) early afterglows has been ushered in. Very early optical/IR detections have been made with ground-based telescopes (Akerlof et al. 1999; Fox et al. 2003; Li et al. 2003a; Blake et al. 2005; Vestrand et al. 2005) before and during the initial operation of *Swift*. In the X-ray band, some evidence of the early afterglows has been collected earlier (e.g., Piro et al. 1998; Giblin et al. 1999; Burenin et al. 1999; Piro et al. 2005). However, it is the operation of the *Swift* X-Ray Telescope (XRT) that offers the possibility to unveil the final gap between the prompt emission and the late afterglow stage.

There has been widespread expectation that the early X-ray observations could answer a series of core questions in GRB studies. What is the connection between the GRB prompt emission and the afterglow? Are prompt emission and afterglow both from the external shock (Mészáros & Rees 1993; Dermer &

Mitman 1999) or do they come from different locations (i.e., prompt emission from the internal shocks [Rees & Mészáros 1994; Paczynski & Xu 1994], while the afterglow comes from the external shock [Mészáros & Rees 1997a; Sari et al. 1998])? Does the central engine become dormant after the burst is over? What is the immediate environment of the burst, an interstellar medium (ISM) or a wind? Are there density clumps surrounding the GRB progenitor? What is the role of the reverse shock? What is the initial Lorentz factor of the fireball?

All of these questions can be at least partially answered with the early X-ray afterglow data, sometimes in combination with the prompt gamma-ray data and the early optical/IR afterglow data. Although early afterglow light curves have been extensively modeled in the optical band (mainly driven by the observations and by the theoretical argument that the reverse shock emission component plays an important role in the optical band; e.g., Mészáros & Rees 1997a, 1999; Sari & Piran 1999; Kobayashi 2000; Kobayashi & Zhang 2003a, 2003b; Zhang et al. 2003; Wei 2003; Wu et al. 2003; Li et al. 2003b; Fan et al. 2004a, 2005b, 2005c; Zhang & Kobayashi 2005; Nakar & Piran 2004; McMahon et al. 2004), possible early X-ray afterglow signatures have been only sparsely studied (e.g., Kumar & Panaitescu 2000b; Kobayashi et al. 2005; Fan & Wei 2005).

In its first 6 months of operations, the *Swift* XRT has already accumulated a rich collection of early afterglow features in the X-ray band. The XRT is a sensitive broadband (0.2–10 keV) imager, which can be promptly slewed to GRB targets triggered by the Burst Alert Telescope (BAT) within 1–2 minutes (Burrows et al. 2005b). It is therefore an ideal instrument to study the transition between the GRB prompt emission and the very early X-ray afterglow. The following features are all detected by XRT in a good sample of bursts (for a collection of data see, e.g.,

¹ Department of Physics, University of Nevada, 4505 South Maryland Parkway, Las Vegas, NV 89154.

² Purple Mountain Observatory, Chinese Academy of Science, 2 Beijing Xi Lu, Nanjing, Jiangsu 210008, China.

³ National Astronomical Observatories, Chinese Academy of Sciences, A20 Datun Road, Chaoyang Beijing 100012, China.

⁴ Nicolaus Copernicus Astronomical Center, Laboratory for Astrophysics I, Ul. Rabianska 8, 87-100 Torun, Poland.

⁵ Department of Astronomy and Astrophysics, Pennsylvania State University, 525 Davey Laboratory, University Park, PA 16802.

⁶ Department of Physics, Pennsylvania State University, 104 Davey Laboratory, University Park, PA 16802.

⁷ Astrophysics Research Institute, Liverpool John Moores University, Twelve Quays House, Birkenhead CH41 1LD, UK.

⁸ NASA Goddard Space Flight Center, Greenbelt, MD 20771.

Chincarini et al. 2005; Nousek et al. 2006), reflecting some common underlying physics of GRBs:

1. In most cases (e.g., GRB 050126 and GRB 050219A), a steep decay is observed up to several hundred seconds after the burst trigger, which is followed by a more conventional, shallower decay (Tagliaferri et al. 2005; Goad 2006). This conclusion is drawn by choosing the GRB trigger time as the zero time point (t_0). At later times (e.g., $t - t_0 \gg T_{90}$, where T_{90} is the duration of the GRB), the afterglow decay slope $d \ln F_\nu / d \ln (t - t_0)$ is essentially independent of the adopted t_0 . However, at early times (e.g., $t - t_0$ not much larger than T_{90}), the measured decay slope could be very sensitive to the assumed t_0 . Tagliaferri et al. (2005) explored the t_0 effect and concluded that the two distinct light-curve segments are likely intrinsic rather than due to a poor choice of t_0 . Furthermore, in some cases, the steep decay segment also has a different spectral index (e.g., for GRB 050319; Cusumano et al. 2006). Usually it also connects to the spectral extrapolation of the BAT prompt emission light curve smoothly (Barthelmy et al. 2005a). All of these facts indicate that the steep decay component is a distinct new component that may be unrelated to the conventional afterglow component.

2. In a good fraction of GRBs (e.g., GRB 050128, Campana et al. 2005; GRB 050315, Vaughan et al. 2006; GRB 050319, Cusumano et al. 2006; GRB 050401, De Pasquale et al. 2006), the early X-ray afterglow is characterized by a shallow-to-“normal” transition. During the transition the spectral index is not changed. The decay slope after the break (e.g., approximately -1.2) is consistent with the standard ISM afterglow model, while the decay slope before the break is usually much shallower (e.g., approximately -0.5).

3. In some cases (e.g., GRB 050315; Vaughan et al. 2006), a further steepening is detected after the normal decay phase, which is consistent with a jet break.

4. Bright X-ray flares have been detected in the early X-ray light curves of nearly one-half of the burst population (e.g., GRB 050406, GRB 050202B; Burrows et al. 2005a; Romano et al. 2006; Falcone et al. 2006). In particular, the X-ray afterglow of the short-hard burst GRB 050724 also shows at least three flares (Barthelmy et al. 2005b). The flares typically happen hundreds of seconds after the trigger or earlier, but in some cases they occur around a day after the trigger (e.g., GRB 050502B, Falcone et al. 2006; GRB 050724, Barthelmy et al. 2005b). The amplitudes of the flares are usually larger than the underlying afterglow component by a factor of several (e.g., a factor of 6 in GRB 050406; Burrows et al. 2005a; Romano et al. 2006) but can be much larger (e.g., ~ 500 in the case of GRB 050202B; Burrows et al. 2005a; Falcone et al. 2006). A similar feature was evident for GRB 011121 detected by *BeppoSAX* (Piro et al. 2005).

In summarizing the current X-ray afterglow data, one can tentatively draw a synthetic cartoon light curve in the X-ray band, which consists of five components (see Fig. 1): (I) an initial steep decay (with a typical slope approximately -3 or steeper); (II) a shallower than normal decay (with a typical slope approximately -0.5); (III) a normal decay (with a typical slope approximately -1.2); (IV) a late steeper decay (with a typical slope approximately -2); and (V) one or more X-ray flares. We note that Nousek et al. (2006) also arrived at a similar schematic diagram that includes the segments I, II, and III in our cartoon picture (see their Fig. 3). Limited by the quality of the data, the current analyses indicate that the spectral indices remain unchanged in segments II, III, and IV, with a typical value of $\beta_X \sim 1$ ($F_X \propto \nu^{-\beta_X}$; Nousek et al. 2006). In some bursts, segments I and II have different spectral indices (e.g., GRB 050319; Cusumano et al.

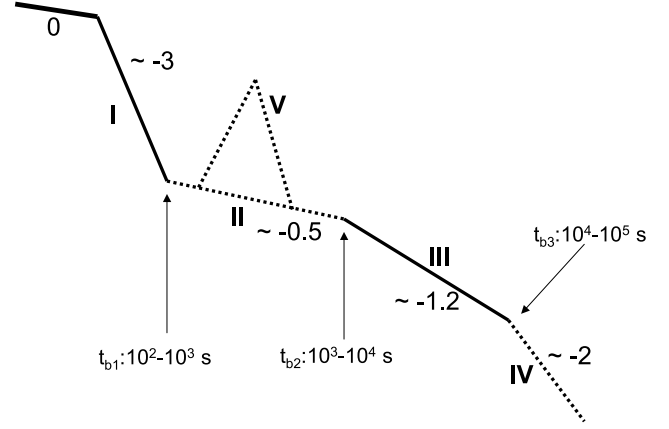


FIG. 1.—Synthetic cartoon X-ray light curve based on the observational data from the *Swift* XRT. The phase “0” denotes the prompt emission. Four power-law light-curve segments together with a flaring component are identified in the afterglow phase. Segments I and III are most common, and they are marked with solid lines. The other three components are only observed in a fraction of bursts, so they are marked as dashed lines. Typical temporal indices in the four segments are indicated in the figure. The spectral indices remain unchanged for segments II, III, and IV, with a typical value of $\beta_X \sim 1$ ($F_X \propto \nu^{-\beta_X}$). Segment I sometimes has a softer spectrum (e.g., $\beta_X \sim 1.5$), but in some other cases it has a similar spectral index as the other three segments. The flares (segment V) have similar spectra as segment I, and time evolution of the spectral index during the flares has been observed in some bursts (e.g., GRB 050502B).

2006). In some cases, a time evolution of the spectral index has been detected (e.g., in the giant flare of GRB 050502B; Falcone et al. 2006). In Figure 1 we have indicated the typical temporal index for each segment. Throughout the paper the transition times between the adjacent segments for the four light-curve segments are denoted as t_{b1} , t_{b2} , and t_{b3} , respectively.

In this paper we systematically study the physical processes that shape an early X-ray light curve and discuss possible theoretical interpretations of the above phenomena. In § 2 we discuss the GRB tail emission arising from high angular latitude relative to the viewing direction, which takes longer to reach the observer due to the extra distance it travels, as a conical (or spherical) shell suddenly stops shining. This is the so-called curvature effect (Fenimore et al. 1996; Kumar & Panaitescu 2000b; Dermer 2004; Dyks et al. 2005). In § 3 we review the main emission properties from the external forward shock region in the X-ray band, summarizing the temporal and spectral indices expected in the X-ray band for both the ISM and the wind models. Furthermore, we also discuss the case of a continuously refreshed shock and its three possible physical mechanisms. Several case studies are investigated to reveal an intriguing refreshed shock phase commonly present in many bursts. In § 4 we briefly discuss whether and how the reverse shock emission would influence the X-ray band emission. In § 5 we explore various mechanisms that might give rise to the X-ray flares observed in many bursts (e.g., GRB 050406 and GRB 050202b) and conclude that the phenomenon is best interpreted as due to a late central engine activity. Our conclusions are summarized in § 6.

2. GRB TAIL EMISSION AND THE CURVATURE EFFECT

2.1. GRB Tail Emission

The temporal bridge between the GRB prompt emission and the afterglow emission is essential for revealing whether the prompt emission and the afterglow originate from the same component. The earliest GRB relativistic shock model invoked the external shock as the site for prompt gamma-ray emission (Rees

& Mészáros 1992; Mészáros & Rees 1993). The rapid variability observed in many GRBs is in great contrast with the intuitive expectations in the external shock model, which generally predicts a smooth burst temporal profile, and it has been argued that the radiative efficiency is too low for the model so that a much larger energy budget is required (Sari & Piran 1997). Dermer & Mitman (1999, 2004) argued that if the GRB ambient medium is sufficiently clumpy, an external shock GRB model could reproduce the observed variability with a high-energy efficiency. Within such a picture, the prompt emission and the afterglow originate from the same component (i.e., the external shock), and it is expected that the two emission components are likely smoothly connected in the early phase.

On the other hand, it is now commonly believed that GRB prompt emission originates from some “internal processes,” i.e., the gamma rays are emitted before the fireball is decelerated by the ambient medium. The most widely discussed model is the internal shock model (Rees & Mészáros 1994; Paczynski & Xu 1994; Kobayashi et al. 1997; Daigne & Mochkovitch 1998; Fan et al. 2004b). Alternatively, the internal emission may be caused by dissipation of strong magnetic fields (e.g., Drenkhahn & Spruit 2002) or Comptonization of the photospheric emission (Rees & Mészáros 2005). Within such scenarios, there exist two distinct temporal episodes dominated by the prompt emission and the afterglow, respectively, since the latter is emitted at a much larger distance from the central engine when the fireball is decelerated. Generally one should expect a flux contrast between these two episodes.

Before the *Swift* era, no solid observation was available to finally differentiate both scenarios, and evidence in favor of each scenario had been collected (for a review see, e.g., Zhang & Mészáros 2004). It is one of the major tasks of *Swift* to pin down the emission site of the GRB prompt emission.

If the prompt emission and the afterglow arise from different emission sites, as is expected in the internal shock (or similar) scenario, and if the prompt emission flux level is much higher than the afterglow emission flux level, one expects to see a steeply decaying light curve during the transition from the prompt emission phase to the afterglow phase. Such a steep decay is due to the so-called curvature effect (e.g., Kumar & Panaitescu 2000b; Dermer 2004; Dyks et al. 2005; Panaitescu et al. 2006). In principle, such an effect also applies to the tail emission of the X-ray flares (Burrows et al. 2005a). Hereafter we generally define such an emission component as “GRB tail emission.”

2.2. Curvature Effect

2.2.1. The Simplest Case

For a conical jet with an opening angle θ_j , emission from the same radius R_{cr} but from different viewing latitudes θ ($\theta < \theta_j$) would reach the observer at different times. Even if the emission is turned off instantaneously, due to the propagation effect the observer would receive the emitted photons at the angle θ at $t = (1 + z)(R_{\text{cr}}/c)(\theta^2/2)$. Such a tail emission thus lasts for a duration of

$$t_{\text{tail}} = (1 + z)(R_{\text{cr}}/c)\left(\frac{\theta_j^2}{2}\right) \simeq (330 \text{ s}) \left(\frac{R_{\text{cr}}\theta_j^2}{10^{13} \text{ cm rad}^2}\right) \left(\frac{1 + z}{2}\right) \quad (1)$$

if the line of sight is not too close to the jet edge.

We consider the simplest case of a jet moving with a constant bulk Lorentz factor Γ (or a constant velocity v). The electrons are

shock heated up to a radius R_{cr} , beyond which no fresh shocked electrons are injected, and the already heated electrons cool rapidly. The comoving emission frequency ν' is boosted to $\nu = \mathcal{D}\nu'$ in the observer's frame, where $\mathcal{D} = [\Gamma(1 - v \cos \theta/c)]^{-1}$ is the Doppler factor, which is $\mathcal{D} \sim 2\Gamma$ for $\theta \ll 1/\Gamma$ and $\mathcal{D} \sim 2/(\Gamma\theta^2)$ for $\theta \gg 1/\Gamma$. Since $t \propto \theta^2$, one gets $\mathcal{D} \propto t^{-1}$ for $\theta \gg 1/\Gamma$.

The observed flux F_ν is related to the comoving surface brightness $L'_{\nu'}$ by

$$F_\nu \propto L'_{\nu'} \mathcal{D}^2 \propto (\nu')^{-\beta} \mathcal{D}^2 \propto \nu^{-\beta} \mathcal{D}^{2+\beta} \propto \nu^{-\beta} t^{-2-\beta}, \quad (2)$$

where β is the observed spectral index around the observed frequency ν , and the last proportionality is valid for $1/\Gamma \ll \theta < \theta_j$. With the standard convention $F_\nu \propto \nu^{-\beta} t^{-\alpha}$, one has the well-known result for the curvature effect (e.g., Kumar & Panaitescu 2000b; Dermer 2004; Fan & Wei 2005; Dyks et al. 2005; Panaitescu et al. 2006)

$$\alpha = 2 + \beta. \quad (3)$$

2.2.2. Emission from a Decelerating Fireball

In reality, the Lorentz factor of the shell could be decreasing right before the sudden cessation of the emission. This is valid for the external shock case in the deceleration phase, or even in the internal shock case. We perform numerical calculations to investigate such an effect.⁹ The curvature effect for the sudden switching off of radiation in a decelerating outflow is presented in Figure 2, in which we plot the X-ray light curve from an expanding jet blast wave with $E_{\text{iso}} = 10^{52}$ ergs, $\Gamma_0 = 240$, $\theta_j = 0.1$, $n = 1 \text{ cm}^{-3}$, and $z = 1$. We manually turn off the radiation at radii (R_{cut}) of 10^{16} , 3×10^{16} , and 6×10^{16} cm, respectively, and investigate the subsequent curvature effect. The radiation from fluid elements at $R < R_{\text{cut}}$ has been rigorously integrated. The result indicates that the $\alpha = 2 + \beta$ conclusion is essentially unchanged.

2.2.3. Jet Structure Effects

Another interesting issue is the jet structure. In principle, GRB jets could be structured (Zhang & Mészáros 2002b; Rossi et al. 2002; Zhang et al. 2004a; Kumar & Granot 2003). Since the curvature effect allows one to see the high-latitude emission directly, an interesting question is whether the decay slope associated with the curvature effect depends on the unknown jet structure. We have investigated this effect with the first code and find that for a relativistic outflow the temporal slope of the curvature effect is largely insensitive to the jet structure as long as the viewing angle is not far off the bright beam. The main reason

⁹ In this paper we use two codes to perform numerical calculations. The first code was developed by J. Dyks (Dyks et al. 2005). The code can deal with the afterglow emission of an outflow with an arbitrary axisymmetric structure and an arbitrary observer's viewing direction. The dynamics of the radial outflow is modeled similar to Granot & Kumar (2003). Only synchrotron radiation is taken into account at the moment, and synchrotron self-absorption (which is irrelevant for X-ray emission) is ignored. The synchrotron emissivity in the comoving frame is calculated by integration of the synchrotron spectrum over the electron energy distribution. The latter is calculated by solving the continuity equation with the power-law source function $Q = K\gamma^{-p}$, normalized by a local injection rate (Moderski et al. 2000). The electrons cool down through synchrotron radiation and adiabatic expansion. All kinematic effects that affect the observed flux (e.g., Doppler boost, propagation time effects) have been taken into account rigorously, following Salmonson (2003). The second code was developed by Y. Z. Fan. This is an afterglow code developed from the dynamical model of Huang et al. (2000) and has been used in several previous studies (e.g., Fan et al. 2004a, 2005b). The latest addition is to also include the kinetic evolution of the electron distribution (Moderski et al. 2000). We have used both codes in various calculations in this paper, and the results are consistent with each other. The figures presented in this paper are all generated from the second code.

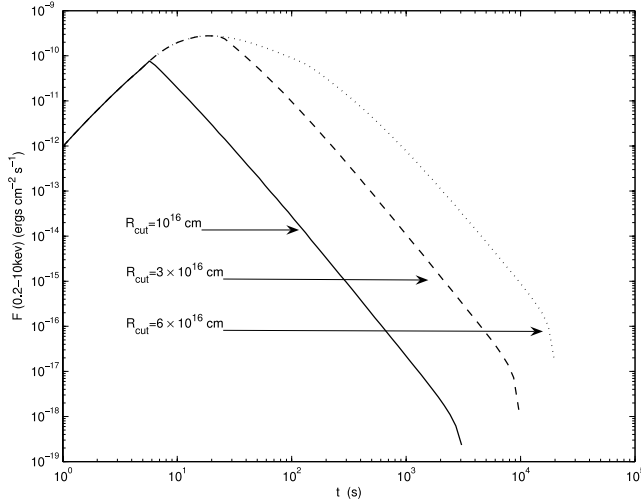


FIG. 2.—Curvature effect for a decelerating ejecta. In the calculation, the radiation from the fluid elements on the equal arrival time surface for $R > R_{\text{cut}}$ is cut out, and the radiation from all other fluid elements is integrated. Here $R_{\text{cut}} = 10^{16}$, 3×10^{16} , and 6×10^{16} cm are the radii at which the radiation is assumed to terminate abruptly. Notice the insensitivity of the decay slope ($\alpha = 2 + \beta$) on the cutoff radius. The following parameters are adopted: the isotropic kinetic energy $E_{\text{iso}} = 10^{52}$ ergs, the initial Lorentz factor $\Gamma_0 = 240$, the jet half-opening angle $\theta_j = 0.1$, the ambient density $n = 1 \text{ cm}^{-3}$, the redshift $z = 1$ (the luminosity distance $D_L = 2.2 \times 10^{28}$ cm), the electron spectral index $p = 2.3$, and the electron and magnetic equipartition parameters $\epsilon_e = 0.1$ and $\epsilon_B = 0.01$, respectively.

is that the decrease of flux because of the curvature effect occurs on a much shorter timescale than that for the jet structure to take effect. For a spectral index $-\beta$ ($f_\nu \propto \nu^{-\beta}$), the flux decreases by m orders of magnitude after a time of $t_{\text{crv}} = 10^{m/(2+\beta)} t_{\text{cr}}$, where t_{cr} is the observer time at which the curvature effect began. For a typical $\beta \sim 1$, the flux drops by 1 order of magnitude after a short time $t_{\text{crv}} \sim 2t_{\text{cr}}$. A drop of 3 orders of magnitude occurs in no more than a decade in time. On the other hand, the observer can perceive the switch-off of emissivity at an angle θ measured from the line of sight at a time $t_\theta \simeq [1 + (\theta\Gamma)^2] t_{\text{cr}}$. One can see that the structure of the outflow must have a typical angular scale smaller than $3/\Gamma$ in order to affect the observed flux before $10t_{\text{cr}}$. For $\Gamma > 10^2$, the parameters of the outflow would have to vary strongly on a scale smaller than 1° . Nonetheless, the effect of the jet structure would start to play a noticeable role if the line of sight is outside the bright beam. Detailed calculations are presented elsewhere (Dyks et al. 2005).

2.2.4. Factors Leading to Deviations from the $\alpha = 2 + \beta$ Relation

Almost all of the *Swift* XRT early afterglow light curves are categorized by a steep decay component followed by a more normal decaying afterglow light curve (Tagliaferri et al. 2005; Nousek et al. 2006; see segment I in Fig. 1). In most of these cases, the measured α - and β -values in this rapidly decaying component are close to the $\alpha = 2 + \beta$ relation but do not match completely. This does not invalidate the curvature effect interpretation, however, since in principle the following factors would lead to deviations from the simple $\alpha = 2 + \beta$ law:

1. The time zero point (t_0) effect. In GRB studies, the afterglow light curves are plotted in the log-log scale, with $t_0 = 0$ defined as the trigger time of the burst. When discussing the late afterglows, shifting t_0 by the order of the burst duration T_{90} does not make much difference. When discussing the early afterglow and its connection to the prompt emission, however, the decay power-law index $[d \ln F_\nu / d \ln (t - t_0)]$ is very sensitive to the

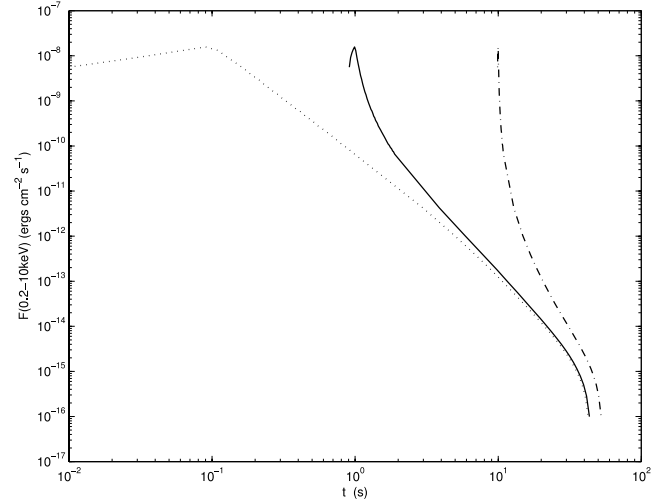


FIG. 3.—Effect of t_0 on the light curves. The same internal shock gamma-ray pulse is calculated but is assigned to three different ejection times t_{ej} . The dotted, solid, and dot-dashed lines are for $t_{\text{ej}} = 0.0$, 1.0, and 10.0 s, respectively. The following parameters are adopted to calculate the internal shock pulses: the pulse luminosity $L_{\text{pulse}} = 10^{51}$ ergs s^{-1} , the variability timescale $\delta t = 0.1$ s, $\theta_j = 0.2$ rad, $\epsilon_e = 0.5$, $\epsilon_B = 0.1$, $p = 2.5$, and $z = 1$.

t_0 value one chooses. Correctly choosing t_0 is therefore essential to derive the correct temporal decay index α . In the case of the internal shock model, the case is straightforward. The observed pulses essentially track the behavior of the central engine (Kobayashi et al. 1997). Each pulse marks another restart of the central engine, so that t_0 should be redefined for each pulse when the curvature effect of that pulse is considered. Keeping the same t_0 as the beginning of the first pulse (i.e., the GRB trigger) would inevitably lead to a false, very steep power-law decay for later pulses. Figure 3 gives an example to show this point. When a series of shells are successively ejected, each pulse will be followed by its tail emission due to the curvature effect, but most of these tails are buried under the main emission of the next pulse. The observed curvature effect is only the tail emission of the very last pulse. As a result, properly shifting t_0 is essential to interpret the steep decay component observed in XRT bursts.

2. The superposition effect. The observed steep-to-shallow transition in the early phase of XRT bursts (Tagliaferri et al. 2005) suggests that by the end of the tail emission, the fireball is already decelerated, and the forward shock emission also contributes to the X-ray band. As a result, the observed steep decay should also include the contribution from the forward shock. Assuming that the latter has a temporal decay index $-w$, the X-ray flux at the early phase should read

$$F_\nu(t) = A \left(\frac{t - t_{0,i}}{t_{0,i}} \right)^{-(2+\beta)} + B \left(\frac{t - t_{0,e}}{t_{0,e}} \right)^{-w}, \quad (4)$$

where A and B are constants and $t_{0,i}$ and $t_{0,e}$ are the time zero points for the steep decay component (presumably of the internal origin) and for the shallow decay component (presumably of the external origin), respectively. In the intermediate regime between the two power-law segments, both components are important, and the observed α should be shallower than $2 + \beta$ during the steep decaying phase. This effect flattens the decay instead of steepening it.

3. If, with the above two adjustments, the observed α is still steeper than $2 + \beta$, one can draw the conclusion that the solid

angle of the emitting region is comparable to or smaller than $1/\Gamma$. This would correspond to a patchy shell (Kumar & Piran 2000b) or a minijet (Yamazaki et al. 2004). A caveat on such an interpretation is that the probability for the line of sight sitting right on top of such a very narrow patch/minijet is very small. As a result, this model cannot interpret an effect that seems to be a general property of X-ray afterglows.

4. If, with the first two adjustments, the observed α is flatter than $2 + \beta$ but is still much steeper than that expected from a forward shock model, there could be two possibilities. One is that the emission is still from the internal dissipation of energy but the emission in the observational band does not cease abruptly. This is relevant when the observational band is below the cooling frequency. The adiabatic cooling therefore gives a decay slope of $\sim(1 + 3\beta/2)$ rather than $\sim(2 + \beta)$ (e.g., Sari & Piran 1999; Zhang et al. 2003). The second possibility is that one is looking at a structured jet (Zhang & Mészáros 2002b; Rossi et al. 2002), with the line of sight significantly off-axis. The curvature effect in such a configuration typically gives a flatter decay slope than $2 + \beta$ (Dyks et al. 2005). This is particularly relevant for X-ray-rich GRBs or X-ray flashes for which a large viewing angle is usually expected (Zhang et al. 2004a; Yamazaki et al. 2004). Further analyses of XRT data suggest that at least in some GRBs, the decay slope is shallower than $2 + \beta$ (O’Brien et al. 2006). The above two possibilities are in particular relevant for these bursts.

We suggest that most of the rapid-decay light curves observed by the *Swift* XRT may be interpreted as GRB (or X-ray flare) tail emission through the curvature effect, with the first two adjustments discussed above. In order to test this hypothesis, after the submission of this paper we have performed more detailed data analyses on a large sample of XRT bursts (Liang et al. 2006). By assuming that the decay slope should be $2 + \beta$, we search the appropriate t_0 that allows such an assumption to be satisfied. It is found that t_0 is usually at the beginning of the last pulse (for the steep decay following the prompt emission) or at the beginning of the X-ray flare (for steep decay following flares). This fact strongly suggests that the curvature effect is likely to be the correct interpretation and at the same time lends strong support to the internal origin of the prompt emission and X-ray flares (see §§ 2.3 and 5.7 for the arguments in favor of the internal models for both components).

Another potential test of the curvature effect is to search for a correlation between the spectral peak energy (E_{pk}) and the flux at the peak (F_{pk} ; Dermer 2004). This requires a well-measured E_{pk} in the XRT band. In most cases, the XRT spectrum is consistent with a single power law. More detailed analyses on future bright X-ray flares are desirable to perform such a test.

2.3. Theoretical Implications

The current *Swift* XRT observations of the early rapid-to-shallow decay transition of the X-ray light curves (Tagliaferri et al. 2005), when interpreted as the curvature effect, have profound implications for the understanding of the GRB phenomenon:

1. It gives a direct observational proof that the GRB prompt emission very likely comes from a different site than the afterglow emission. This suggests that the emission either comes from the internal shocks due to the collisions among many engine-ejected shells (Rees & Mészáros 1994; Paczynski & Xu 1994) or is due to magnetic or other dissipation processes at a radius smaller than the fireball deceleration radius (e.g., Drenkhahn & Spruit 2002; Rees & Mészáros 2005). In both scenarios, the energy dissipation region is well inside the region where the deceleration of the whole fireball occurs.

2. An interesting fact is that in most cases, after the prompt emission, the X-ray emission level (that spectrally extrapolated from the BAT data) drops by several orders of magnitude (through the curvature effect, in our interpretation) before “landing” on the afterglow emission level. One could roughly estimate the expected “drop-off.” The flux level in the XRT band during the prompt phase could be roughly estimated as $F_{\nu, X}^{\text{prompt}} \propto (E_{\gamma, \text{iso}}/T_{90}) (E_{\text{XRT}}/E_p)^{\hat{\alpha}+2}$, where $E_{\gamma, \text{iso}}$ is the isotropic energy of the emitted gamma rays, T_{90} is the duration of the burst, $E_{\text{XRT}} \sim 5$ keV is the typical energy in the XRT band, $E_p \sim 100$ keV is the typical peak energy in the GRB spectrum, and $\hat{\alpha} \sim -1$ is the low-energy spectral index for a Band spectrum (Band et al. 1993). Assuming that the X-ray band for the afterglow emission is above both the typical synchrotron frequency ν_m and the cooling frequency ν_c (which is usually the case for the ISM model; see eqs. [7] and [8]), the X-ray afterglow flux level can be estimated as (e.g., Freedman & Waxman 2001) $F_{\nu, X}^{\text{ag}} \propto \epsilon_e E_{\text{iso}}/t$, where E_{iso} is the isotropic energy of the afterglow kinetic energy and ϵ_e is the electron equipartition parameter in the shock.¹⁰ The flux contrast can be estimated as

$$\frac{F_{\nu, X}^{\text{prompt}}}{F_{\nu, X}^{\text{ag}}} \sim \left(\frac{E_{\gamma, \text{iso}}}{E_{\text{iso}}} \right) \left(\frac{t}{T_{90}} \right) \left[\frac{(E_{\text{XRT}}/E_p)^{\hat{\alpha}+2}}{\epsilon_e} \right]. \quad (5)$$

For typical parameters, one has $(E_{\text{XRT}}/E_p)^{\hat{\alpha}+2} \sim 0.05$ and $\epsilon_e \sim 0.1$, so that the term in square brackets is $\lesssim 1$. Although $t > T_{90}$ would generally suggest that $F_{\nu, X}^{\text{prompt}}$ should be higher than $F_{\nu, X}^{\text{ag}}$, the large contrast between the two components observed in many bursts is usually not accounted for unless $E_{\gamma, \text{iso}}$ is (much) larger than E_{iso} . This refers to a very high apparent GRB radiation efficiency, even higher than the one estimated using the late X-ray afterglow data (Lloyd-Ronning & Zhang 2004).¹¹ The commonly invoked internal shock model predicts a low-emission efficiency (e.g., Panaitescu et al. 1999; Kumar 1999). Understanding such a high apparent radiation efficiency is therefore desirable (see, e.g., Beloborodov 2000; Kobayashi & Sari 2001).

3. The common steep-to-shallow transition feature indicates that the fireball has already been decelerated at the time when the GRB tail emission fades. Otherwise, one would see an initially rising light curve peaking at the fireball deceleration time. This fact alone sets a lower limit to the initial Lorentz factor of the fireball, since the deceleration time t_{dec} must be earlier than the transition time t_{b1} . The numerical expression is

$$\Gamma_0 \geq 125 \left(\frac{E_{\gamma, \text{iso}, 52}}{\eta_\gamma n} \right)^{1/8} t_{b1, 2}^{-3/8} \left(\frac{1+z}{2} \right)^{3/8}, \quad (6)$$

where $E_{\gamma, \text{iso}}$ is the isotropic gamma-ray energy (which is an observable if the redshift z is known) and $\eta_\gamma = E_{\gamma, \text{iso}}/E_{\text{iso}}$ is a conversion factor between the isotropic afterglow energy E_{iso} and $E_{\gamma, \text{iso}}$. Throughout the paper, the convention $Q_x = Q/10^x$ is adopted in cgs units. Applying the method to the bursts with measured z (Chincarini et al. 2005), we get the lower limits of Γ_0 for several bursts (Table 1). Given the weak dependence on the unknown parameters [i.e., $(\eta_\gamma n)^{-1/8}$], we conclude that the data suggest that GRBs are highly relativistic events with typical Lorentz factors higher than 100. This is an independent method, as compared with previous ones using the high-energy

¹⁰ When the synchrotron self-Compton process dominates the cooling, the discussion could be more complicated.

¹¹ This could be attributed to the shallow decay injection phase (segment II in Fig. 1) as discussed in § 3.2. Because of the injection, the effective E_{iso} in the early epochs is smaller than that in the later epochs. As a result, a larger $F_{\nu, X}^{\text{prompt}} - F_{\nu, X}^{\text{ag}}$ contrast is expected.

TABLE 1
CONSTRAINTS ON THE INITIAL LORENTZ FACTORS OF SEVERAL GRBs

GRB	z	t_{b1} (s)	$E_{\gamma,iso,52}^a$	Γ_0
050126.....	1.290 ^b	~110	0.77	$>120(\eta_\gamma n)^{-1/8}$
050315.....	1.949 ^c	~400	2.77	$>100(\eta_\gamma n)^{-1/8}$
050319.....	3.240 ^d	~400	5.12	$>120(\eta_\gamma n)^{-1/8}$
050401.....	2.900 ^e	~130	27.49	$>220(\eta_\gamma n)^{-1/8}$

^a Chincarini et al. (2005).

^b Berger et al. (2005).

^c Kelson & Berger (2005).

^d Fynbo et al. (2005a).

^e Fynbo et al. (2005b).

spectrum (e.g., Baring & Harding 1997; Lithwick & Sari 2001), the reverse shock data (Sari & Piran 1999; Wang et al. 2000; Zhang et al. 2003), and the superluminal expansion of the radio afterglow source image (Waxman et al. 1998).

3. FORWARD SHOCK EMISSION

After the rapid fading of the GRB tail emission, usually the forward shock emission component gives the main contribution to the early X-ray afterglow light curves. The light-curve shape depends on the density profile of the ambient medium (i.e., ISM or wind). In the “standard” case (i.e., adiabatic evolution with prompt injection of energy), the fireball energy is essentially constant during the deceleration phase. The bulk Lorentz factor $\Gamma \propto R^{-3/2}$ for the ISM case and $\Gamma \propto R^{-1/2}$ for the wind case. When the bulk Lorentz factor Γ is larger than θ_j^{-1} , where θ_j is the jet opening angle (or the viewing angle of a structured jet), the system is simply determined by the ratio of the isotropic afterglow energy E_{iso} and the ambient density n (or the A parameter in the wind model). Such a normal decay phase corresponds to segment III in the synthetic light curve (Fig. 1). When Γ becomes smaller than θ_j^{-1} , the light curve steepens because of the combination of the jet edge effect and the possible sideways expansion effect (Rhoads 1999; Sari et al. 1999; Panaitescu & Mészáros 1999). The bulk Lorentz factor decreases exponentially with radius. This is known as a “jet break,” and the postbreak segment corresponds to segment IV in Figure 1.

During the early evolution of the fireball, the forward shock may be continuously refreshed with additional energy. This could be because of either a continuous operation of the central engine (Dai & Lu 1998a; Zhang & Mészáros 2001; Dai 2004), or a power-law distribution of the Lorentz factors in the ejecta that results in slower ejecta catching up with the decelerated fireball at later times (Rees & Mészáros 1998; Panaitescu et al. 1998; Kumar & Piran 2000a; Sari & Mészáros 2000; Zhang & Mészáros 2002a), or the transferring of the Poynting flux energy to the medium when a Poynting flux-dominated flow is decelerated (e.g., Zhang & Kobayashi 2005). The canonical XRT light curve (Fig. 1) indeed shows a shallow decay phase (segment II), which we argue is due to continuous energy injection.

3.1. Standard Afterglow Models

For the convenience of the later discussion, we summarize the standard early forward shock X-ray afterglow properties as follows:

1. *The ISM model* (e.g., Sari et al. 1998).—The typical synchrotron frequency and the cooling frequency are $\nu_m = (6.5 \times 10^{14} \text{ Hz}) \epsilon_{B,-2}^{1/2} \epsilon_{e,-1}^2 E_{52}^{1/2} t_3^{-3/2} [(1+z)/2]^{1/2}$ and $\nu_c = (2.5 \times 10^{16} \text{ Hz})$

$(1+Y)^{-2} \epsilon_{B,-2}^{-3/2} E_{52}^{-1/2} n^{-1} t_3^{-1/2} [(1+z)/2]^{-1/2}$, respectively, where E is the isotropic kinetic energy of the fireball, n is the ISM density, ϵ_e and ϵ_B are shock equipartition parameters for electrons and magnetic fields, respectively, Y is the energy ratio between the inverse Compton component and the synchrotron component, z is the redshift, and t is the observer’s time. Both frequencies decrease with time. The time interval for ν_m and ν_c to cross the XRT energy band (0.5–10 keV) from above can be expressed as

$$t_m = (4-30 \text{ s}) \epsilon_{B,-2}^{1/3} \epsilon_{e,-1}^{4/3} E_{52}^{1/3} \left(\frac{1+z}{2} \right)^{1/3}, \quad (7)$$

$$t_c = (0.1-40 \text{ s}) (1+Y)^{-4} \epsilon_{B,-2}^{-3} E_{52}^{-1} n^{-2} \left(\frac{1+z}{2} \right)^{-1}. \quad (8)$$

The epoch when the fireball switches from fast cooling ($\nu_c < \nu_m$) to slow cooling ($\nu_c > \nu_m$) is defined by requiring $\nu_m = \nu_c$, which reads

$$t_{mc} = (26 \text{ s}) (1+Y)^2 \epsilon_{B,-2}^2 \epsilon_{e,-1}^2 E_{52} n \left(\frac{1+z}{2} \right). \quad (9)$$

For comparison, the time when the fireball is decelerated (thin-shell case) is given by

$$t_{dec} = \left(\frac{3E}{4\pi n m_p c^2 \Gamma_0^2} \right)^{1/3} \frac{1}{2\Gamma_0^2 c} \\ = (180 \text{ s}) (E_{52}/n)^{1/3} \Gamma_{0,2}^{-8/3} \left(\frac{1+z}{2} \right), \quad (10)$$

where Γ_0 is the initial Lorentz factor of the fireball. We can see that for typical parameters, the XRT band is already in the regime of $\nu_X > \max(\nu_m, \nu_c)$ when deceleration starts. Also, the blast wave evolution has usually entered the slow cooling regime where the radiative losses are not important.¹² Under such conditions, the temporal index is¹³ $\alpha_X = (3p-2)/4 \sim 1.15$, and the spectral index is $\beta_X = p/2 \sim 1.1$ (photon index 2.1). The relation between the two indices is $\alpha_X = (3\beta_X - 1)/2$. In view that t_c is very sensitive to ϵ_B , one can still get the regime $\nu_m < \nu_X < \nu_c$ if $\epsilon_{B,-2}$ is small (say, around 0.1). In such a case, $\alpha_X = 3(p-1)/4 \sim 0.9$, $\beta_X = (p-1)/2 \sim 0.6$, and $\alpha_X = (3/2)\beta_X$. The above two cases have been commonly observed in early X-ray afterglows of many *Swift* bursts (e.g., segment III in Fig. 1), suggesting that the fireball shock model can successfully interpret the general properties of GRB afterglows and that most GRBs are born in a constant-density medium. This conclusion is consistent with previous analyses (Panaitescu & Kumar 2002; Yost et al. 2003).

2. *The wind model* (e.g., Chevalier & Li 2000).—The typical synchrotron frequency and the cooling frequency are $\nu_m = (1.3 \times 10^{15} \text{ Hz}) \epsilon_{B,-2}^{1/2} \epsilon_{e,-1}^2 E_{52}^{1/2} t_3^{-3/2} [(1+z)/2]^{1/2}$ (notice that ν_m in the wind case has the same parameter dependencies as the ISM case but is larger by a factor of ~ 2 ; e.g., Dai & Lu 1998b) and $\nu_c = (6.8 \times 10^{12} \text{ Hz}) (1+Y)^{-2} \epsilon_{B,-2}^{-3/2} E_{52}^{1/2} A_*^{-2} t_3^{1/2} [(1+z)/2]^{-3/2}$, where $A_* = (\dot{M}_W/4\pi V_W)/(5 \times 10^{11} \text{ g cm}^{-1})$ is the typical wind parameter, \dot{M}_W is the mass-loss rate, and V_W is the wind velocity. A distinguishing property of the wind model is that ν_c increases

¹² In certain parameter regimes, the condition $t_{dec} < t_{mc}$ could be satisfied, and in the temporal regime $t < t_{mc}$, the blast wave is in the fast cooling ($\nu_c < \nu_m$) domain, so the radiative loss could affect the blast wave dynamics (e.g., Böttcher & Dermer 2000; Wu et al. 2005).

¹³ Here and below, the convention $F_\nu(X) \propto t^{-\alpha_X} \nu^{-\beta_X}$ is adopted since in the X-ray band both the temporal and the spectral indices are negative. Also $p = 2.2$ is adopted for typical numerical values.

with time. Similarly, the time interval for ν_m to cross the XRT band from above is

$$t_m = (6.6-49 \text{ s}) \epsilon_{B,-2}^{1/3} \epsilon_{e,-1}^{4/3} E_{52}^{1/3} \left(\frac{1+z}{2} \right)^{1/3}, \quad (11)$$

and the time interval for ν_c to cross the band from below is

$$\begin{aligned} t_c &= (3.1 \times 10^{11} - 1.2 \times 10^{14} \text{ s}) (1+Y)^4 \epsilon_{B,-2}^3 E_{52}^{-1} A_*^4 \left(\frac{1+z}{2} \right)^3 \\ &= (0.3-120 \text{ s}) (1+Y)^4 \epsilon_{B,-2}^3 E_{52}^{-1} A_{*, -3}^4 \left(\frac{1+z}{2} \right)^3. \end{aligned} \quad (12)$$

The critical time for the fast-slow cooling transition is

$$\begin{aligned} t_{mc} &= (1.4 \times 10^4 \text{ s}) (1+Y) \epsilon_{e,-1} \epsilon_{B,-2} A_* \\ &= (14 \text{ s}) (1+Y) \epsilon_{e,-1} \epsilon_{B,-2} A_{*, -3}. \end{aligned} \quad (13)$$

The deceleration time is essentially the duration of the burst, i.e., $t_{\text{dec}} \sim T = (20 \text{ s}) T_{1.3}$, since for typical parameters the wind model is the so-called thick-shell case (e.g., Chevalier & Li 2000; Kobayashi & Zhang 2003b). For a typical wind parameter $A_* \sim 1$, the X-ray light curve is very simple. For $t < t_m$, one has $\nu_c < \nu_X < \nu_m$, so that $\alpha_X = \frac{1}{4}$, $\beta_X = \frac{1}{2}$, and $\alpha_X = (1 - \beta_X)/2$. When $t > t_m$, during most of the observational time of interest, one has $\nu_X > \max(\nu_m, \nu_c)$, so that $\alpha_X = (3p - 2)/2 \sim 1.15$, $\beta_X = p/2 = 1.1$ (photon index 2.1), and $\alpha_X = (3\beta_X - 1)/2$. The switching between the fast cooling and slow cooling regimes does not influence the temporal and spectral indices in the X-ray band. Only when $A_* < 0.01$, i.e., t_c falls into the range of observational interest, does a new temporal/spectral domain appear. When $t > t_c$, one has $\nu_m < \nu_X < \nu_c$, $\alpha_X = (3p - 1)/4 \sim 1.4$, $\beta_X = (p - 1)/2 \sim 0.6$ (photon index 1.6), and $\alpha_X = (3\beta_X + 1)/2$. Such a feature has been used to interpret GRB 050128 (Campana et al. 2005).¹⁴ If A_* is not much smaller than unity, the blast wave is in the fast cooling regime, and radiative losses could be substantial (Böttcher & Dermer 2000). A detailed analysis has been presented in Wu et al. (2005).

3. *The jet model* (e.g., Rhoads 1999; Sari et al. 1999).—After the jet break, the temporal decay index is predicted to be $\alpha_X = p$. This is derived by assuming significant sideways expansion. This result is independent of whether the X-ray band is below or above ν_c and whether the medium is an ISM or a stellar wind. For the latter, the timescale for the light curve to achieve the asymptotic $-p$ index is typically longer than that in the ISM case (e.g., Kumar & Panaitescu 2000a; Gou et al. 2001).

All of the above discussions apply for the case of $p > 2$. For $p < 2$, the case could be different. Dai & Cheng (2001) proposed one scenario to deal with the case of $p < 2$, while Panaitescu & Kumar (2002) extended the treatment of the $p > 2$ case to the $p < 2$ regime.

3.2. Refreshed Shock Models

If there is significant continuous energy injection into the fireball during the deceleration phase, the forward shock keeps being “refreshed,” so that it decelerates less rapidly than in the standard case. The bulk Lorentz factor of the fireball decays more slowly than $\Gamma \propto R^{-3/2}$ ($\Gamma \propto R^{-1/2}$) for the ISM (wind) case.

There are three possible physical origins for the refreshed shocks:

1. The central engine itself is longer lasting, e.g., behaving as

$$L(t) = L_0(t/t_b)^{-q}. \quad (14)$$

The dynamical evolution and the radiation signature of such a system have been discussed in detail in Zhang & Mészáros (2001). A specific model for such an injection case, i.e., the energy injection from the initial spin-down from a millisecond pulsar (preferably a millisecond magnetar), was discussed in that paper and earlier in Dai & Lu (1998a). In such a specific model, $q = 0$ is required according to the spin-down law. Alternatively, the continued engine activity could be due to continued infall onto a central black hole, resulting in the time dependence equation (14).¹⁵ In general, for an adiabatic fireball, the injection would modify the blast wave dynamics as long as $q < 1$ (Zhang & Mészáros 2001). The energy in the fireball increases with time as $E_{\text{iso}} \propto t^{1-q}$, so that

$$\Gamma \propto R^{-(2+q)/2(2-q)} \propto t^{-(2+q)/8}, \quad R \propto t^{(2-q)/4}, \quad (15)$$

$$\Gamma \propto R^{-q/2(2-q)} \propto t^{-q/4}, \quad R \propto t^{(2-q)/2}, \quad (16)$$

for the ISM and wind models, respectively. It is then straightforward to work out the temporal indices for various temporal regimes.

The ISM model.—The typical synchrotron frequency $\nu_m \propto \Gamma^2 \gamma_e B \propto \Gamma^4 \propto t^{-(2+q)/2}$, the synchrotron cooling frequency $\nu_c \propto \Gamma^{-1} B^{-3} t^{-2} \propto \Gamma^{-4} t^{-2} \propto t^{(q-2)/2}$, and the peak flux density $F_{\nu, \text{max}} \propto N_e B \Gamma \propto t^{1-q}$, where $B \propto \Gamma$ is the comoving magnetic field strength, $\gamma_e \propto \Gamma$ is the typical electron Lorentz factor in the shocked region, and $N_e \propto R^3$ is the total number of the emitting electrons. The temporal indices α for various spectral regimes and their relationships with the spectral indices $\alpha(\beta)$ are listed in Table 2.

The wind model.—In the wind case, the ambient density is $n \propto R^{-2}$, where R is the radial distance of the shock front to the central source. The typical synchrotron frequency $\nu_m \propto \Gamma^2 \gamma_e B \propto \Gamma^3 B \propto t^{-(2+q)/2}$, the synchrotron cooling frequency $\nu_c \propto \Gamma^{-1} B^{-3} t^{-2} \propto \Gamma^{-4} t^{-2} \propto t^{(2-q)/2}$, and the peak flux density $F_{\nu, \text{max}} \propto N_e B \Gamma \propto \Gamma^2 \propto t^{-q/2}$, where $B \propto \Gamma R^{-1}$ is the comoving magnetic field strength and $N_e \propto R$ is the total number of emitting electrons. The temporal indices α for various spectral regimes and their relationships with the spectral indices $\alpha(\beta)$ are listed in Table 2.

In order for the central engine to continuously feed the blast wave, the Lorentz factor of the continuous flow must be (much) larger than that of the blast wave. It could be a Poynting flux-dominated flow. This is not difficult to satisfy since the blast wave keeps decelerating. There could be a reverse shock propagating into the continuous ejecta, but the radiation signature of the reverse shock is typically not in the X-ray band (e.g., Zhang & Mészáros 2001).

2. The central engine activity may be brief (e.g., as brief as the prompt emission itself), but at the end of the prompt phase, the ejecta has a range of Lorentz factors, e.g., the amount of ejected mass moving with Lorentz factors greater than γ is (Rees & Mészáros 1998; Panaitescu et al. 1998; Sari & Mészáros 2000)

$$M(>\gamma) \propto \gamma^{-s}. \quad (17)$$

¹⁴ As discussed in § 3.2, after collecting more data, we now believe that the shallow-to-normal decay observed in GRB 050128 is more likely due to the transition from the energy injection phase to the standard phase (without injection).

¹⁵ The black hole torus system typically has $q = 5/3$ at later times (MacFadyen et al. 2001; Janiuk et al. 2004), which has no effect on the blast wave evolution.

TABLE 2
TEMPORAL INDEX α AND SPECTRAL INDEX β IN VARIOUS AFTERGLOW MODELS

GRB MODELS	β	NO INJECTION		INJECTION	
		α	$\alpha(\beta)$	α	$\alpha(\beta)$
ISM, Slow Cooling					
$\nu < \nu_m$	$\frac{1}{3}$	$\frac{1}{2}$	$\alpha = \frac{3\beta}{2}$	$\frac{5q-8}{6} (-0.9)$	$\alpha = (q-1) + \frac{(2+q)\beta}{2}$
$\nu_m < \nu < \nu_c$	$\frac{p-1}{2} (0.65)$	$\frac{3(p-1)}{4} (1.0)$	$\alpha = \frac{3\beta}{2}$	$\frac{(2p-6)+(p+3)q}{4} (0.3)$	$\alpha = (q-1) + \frac{(2+q)\beta}{2}$
$\nu > \nu_c$	$\frac{p}{2} (1.15)$	$\frac{3p-2}{4} (1.2)$	$\alpha = \frac{3\beta-1}{2}$	$\frac{(2p-4)+(p+2)q}{4} (0.7)$	$\alpha = \frac{q-2}{2} + \frac{(2+q)\beta}{2}$
ISM, Fast Cooling					
$\nu < \nu_c$	$\frac{1}{3}$	$\frac{1}{6}$	$\alpha = \frac{\beta}{2}$	$\frac{7q-8}{6} (-0.8)$	$\alpha = (q-1) + \frac{(2-q)\beta}{2}$
$\nu_c < \nu < \nu_m$	$\frac{1}{2}$	$\frac{1}{4}$	$\alpha = \frac{\beta}{2}$	$\frac{3q-2}{4} (-0.1)$	$\alpha = (q-1) + \frac{(2-q)\beta}{2}$
$\nu > \nu_m$	$\frac{p}{2} (1.15)$	$\frac{3p-2}{4} (1.2)$	$\alpha = \frac{3\beta-1}{2}$	$\frac{(2p-4)+(p+2)q}{4} (0.7)$	$\alpha = \frac{q-2}{2} + \frac{(2+q)\beta}{2}$
Wind, Slow Cooling					
$\nu < \nu_m$	$\frac{1}{3}$	0	$\alpha = \frac{3\beta+1}{2}$	$\frac{q-1}{3} (-0.2)$	$\alpha = \frac{q}{2} + \frac{(2+q)\beta}{2}$
$\nu_m < \nu < \nu_c$	$\frac{p-1}{2} (0.65)$	$\frac{3p-1}{4} (1.5)$	$\alpha = \frac{3\beta+1}{2}$	$\frac{(2p-2)+(p+1)q}{4} (1.1)$	$\alpha = \frac{q}{2} + \frac{(2+q)\beta}{2}$
$\nu > \nu_c$	$\frac{p}{2} (1.15)$	$\frac{3p-2}{4} (1.2)$	$\alpha = \frac{3\beta-1}{2}$	$\frac{(2p-4)+(p+2)q}{4} (0.7)$	$\alpha = \frac{q-2}{2} + \frac{(2+q)\beta}{2}$
Wind, Fast Cooling					
$\nu < \nu_c$	$\frac{1}{3}$	$\frac{2}{3}$	$\alpha = \frac{1-\beta}{2}$	$\frac{(1+q)}{3} (0.5)$	$\alpha = \frac{q}{2} - \frac{(2-q)\beta}{2}$
$\nu_c < \nu < \nu_m$	$\frac{1}{2}$	$\frac{1}{4}$	$\alpha = \frac{1-\beta}{2}$	$\frac{3q-2}{4} (-0.1)$	$\alpha = \frac{q}{2} - \frac{(2-q)\beta}{2}$
$\nu > \nu_m$	$\frac{p}{2} (1.15)$	$\frac{3p-2}{4} (1.2)$	$\alpha = \frac{3\beta-1}{2}$	$\frac{(2p-4)+(p+2)q}{4} (0.7)$	$\alpha = \frac{q-2}{2} + \frac{(2+q)\beta}{2}$

NOTES.—This is the extension of Table 1 of Zhang & Mészáros (2004), with the inclusion of the cases of energy injection. The case of $p < 2$ is not included, and the self-absorption effect is not discussed. Notice that a different convention $F_\nu \propto t^{-\alpha} \nu^{-\beta}$ is adopted here (in comparison to that used in Zhang & Mészáros 2004), mainly because both the temporal index and the spectral index are generally negative in the X-ray band. The temporal indices with energy injection are valid only for $q < 1$, and they reduce to the standard case (without energy injection; e.g., Sari et al. 1998; Chevalier & Li 2000) when $q = 1$. For $q > 1$ the expressions are no longer valid, and the standard model applies. An injection case due to pulsar spin-down corresponds to $q = 0$ (Dai & Lu 1998a; Zhang & Mészáros 2001). Recent *Swift* XRT data are generally consistent with $q \sim 0.5$. The numerical values quoted in parentheses are for $p = 2.3$ and $q = 0.5$.

The total energy in the fireball increases as $E_{\text{iso}} \propto \gamma^{1-s} \propto \Gamma^{1-s}$, so that

$$\Gamma \propto R^{-3/(1+s)} \propto t^{-3/(7+s)}, \quad R \propto t^{(1+s)/(7+s)}, \quad (18)$$

$$\Gamma \propto R^{-1/(1+s)} \propto t^{-1/(3+s)}, \quad R \propto t^{(1+s)/(3+s)}, \quad (19)$$

for the ISM and wind models, respectively. One can then work out the temporal decay indices in various spectral regimes (e.g., Rees & Mészáros 1998; Sari & Mészáros 2000). Alternatively, for each s -value, one can find an effective q -value that mimics the s effect, or vice versa. This gives

$$s = \frac{10-7q}{2+q}, \quad q = \frac{10-2s}{7+s}, \quad (20)$$

$$s = \frac{4-3q}{q}, \quad q = \frac{4}{3+s}, \quad (21)$$

for the ISM and wind models, respectively. In Table 2, the explicit s dependencies are not listed, but they could be inferred from equations (20) and (21).

In this second scenario, the central engine need not last long. All of the material could be ejected promptly. The continuous injection is due to the different velocities of the ejecta. Initially as the blast wave moves with high speed, the slower ejecta lag behind and have no effect on the blast wave evolution. They later progressively pile up onto the blast wave as the latter decelerates. Only when $s > 1$ does one expect a change in the fireball dynamics. This corresponds to $q < 1$. For $q = 0.5$, one gets $s = 2.6$ for the ISM case and $s = 5$ for the wind case.

3. The energy injection is also brief, but the outflow has a significant fraction of Poynting flux (e.g., Usov 1992; Thompson 1994; Mészáros & Rees 1997b; Lyutikov & Blandford 2003). Assigning a parameter σ for the outflow, which is the ratio between the Poynting flux and baryonic kinetic energy flux, Zhang & Kobayashi (2005) modeled the reverse shock emission from ejecta with an arbitrary σ -value. They found that during the crossing of the reverse shock, the Poynting energy is not transferred to the ambient medium. The Poynting energy (roughly by a factor of σ) is expected to be transferred to the medium (and hence, to the afterglow emission) after the reverse shock disappears. Zhang & Kobayashi (2005) suggest that the transfer is delayed with respect

to the traditional case of $\sigma = 0$. The energy transfer process, however, is poorly studied so that one does not have a handy conversion relation with the q -value derived in the first scenario.

3.3. Case Studies

In this subsection we discuss several *Swift* GRBs with well-monitored early afterglow data detected by XRT. The notations for the break times and the temporal slopes are per those marked in Figure 1.

GRB 050128 (Campana et al. 2005).—The light curve can be fitted by a broken power law with the break time at $t_{b2} = 1472^{+300}_{-290}$ s. The temporal decay indices before and after the break are $\alpha_2 = 0.27^{+0.12}_{-0.10}$ and $\alpha_3 = 1.30^{+0.13}_{-0.18}$, respectively. The spectral indices before and after the break are essentially unchanged, i.e., $\beta_2 \sim 0.59 \pm 0.08$ and $\beta_3 = 0.79 \pm 0.11$. Campana et al. (2005) discussed two interpretations. A jet model requires a very flat electron spectral index, i.e., $p \sim 1.3$, as well as a change of the spectral domain before and after the jet break. Alternatively, the data may be accommodated in a wind model, but one has to assume three switches of the spectral regimes during the observational gap from 400 to about 4000 s. So neither explanation is completely satisfactory. By comparing the predicted indices in Table 2, the observation may be well interpreted within the ISM model with an initial continuous energy injection episode. The segment after the break is consistent with a standard ISM model for $\nu_m < \nu_X < \nu_c$, with $p \sim 2.6$. The light curve before the break, on the other hand, is consistent with an injection model with $p \sim 2.2$ and $q \sim 0.5$ in the same spectral regime. The break time is naturally related to the cessation of the injection process, and a slight change of electron spectral index (from 2.2 to 2.6) is required. From the beginning of the observation (100 s) to t_{b2} , the total energy is increased by a factor of $(1472/100)^{(1-0.5)} \sim 3.8$.

GRB 050315 (Vaughan et al. 2006).—After a steep decay ($\alpha_1 = 5.2^{+0.5}_{-0.4}$) up to $t_{b1} = 308$ s, the light curve shows a flat “plateau” with a temporal index of $\alpha_2 = 0.06^{+0.08}_{-0.13}$. It then turns to $\alpha_3 = 0.71 \pm 0.04$ at $t_{b2} = 1.2^{+0.5}_{-0.3} \times 10^4$ s. Finally, there is a third break at $t_{b3} = 2.5^{+1.1}_{-0.3} \times 10^5$ s, after which the temporal decay index is $\alpha_4 = 2.0^{+1.7}_{-0.3}$. So this burst displays all four segments presented in Figure 1. The spectral indices in segments II, III, and IV are essentially constant, i.e., $\beta_2 = 0.73 \pm 0.11$, $\beta_3 = 0.79 \pm 0.13$, and $\beta_4 = 0.7^{+0.5}_{-0.3}$, respectively. Segment III is consistent with an ISM model with $\nu_X > \nu_c$ and $p = 1.6$, since in this model $\beta = p/2 = 0.8$, $\alpha = (3p - 2)/4 = 0.7$, in perfect agreement with the data. The third temporal break t_{b3} is consistent with a jet break. According to Dai & Cheng (2001), the post-break temporal index for $p < 2$ is $\alpha = (p + 6)/4 = 1.9$, which is also consistent with the observed α_4 . The plateau between t_{b1} and t_{b2} is then due to an energy injection in the same ISM model ($\nu_X > \nu_c$), with $p \sim 1.5$ and $q \sim 0.35$. The total injected energy is increased by a factor of $(12,000/308)^{(1-0.35)} \sim 11$.

GRB 050319 (Cusumano et al. 2006).—After a steep decay ($\alpha_1 = 5.53 \pm 0.67$) up to $t_{b1} = 384 \pm 22$ s, the light curve shows a shallow decay with a temporal index of $\alpha_2 = 0.54 \pm 0.04$. It steepens to $\alpha_3 = 1.14 \pm 0.2$ at $t_{b2} = (2.60 \pm 0.70) \times 10^4$ s. The spectral indices in segments II and III are $\beta_2 = 0.69 \pm 0.06$ and $\beta_3 = 0.8 \pm 0.08$, respectively. Again segment III is well consistent with an ISM model for $\nu_m < \nu_X < \nu_c$ with $p = 2.6$, which gives $\beta = (p - 1)/2 = 0.8$ and $\alpha = (3/2)\beta = 1.2$, in excellent agreement with the data. Interpreting segment II (the shallow decay phase) as the energy injection phase, for the same ISM model ($\nu_m < \nu_X < \nu_c$), one gets $p \sim 2.4$ and $q \sim 0.6$. The total injected energy is increased by a factor of $(26,000/384)^{(1-0.6)} \sim 5.4$. The UVOT observations are also consistent with such a picture (Mason et al. 2006).

GRB 050401 (De Pasquale et al. 2006).—The early X-ray light curve is consistent with a broken power law, with $\alpha_2 = 0.63 \pm 0.02$, $\alpha_3 = 1.41 \pm 0.1$, and $t_{b2} = 4480^{+520}_{-440}$ s. The spectral indices before and after the break are all consistent with $\beta_2 \sim \beta_3 = 0.90 \pm 0.03$. The α - β relation does not fit into a simple $p < 2$ jet model. On the other hand, the energy injection model gives a natural interpretation. After the break, the light curve is consistent with an ISM model for $\nu_m < \nu_X < \nu_c$ with $p = 2.8$. Before the break, it is consistent with the same model with $q = 0.5$. The total injected energy is increased by a factor of $>(4480/200)^{(1-0.5)} \sim 4.7$.

The injection signature is also inferred in other bursts such as GRB 050117 (Hill et al. 2006) and XRF 050416 (Sakamoto et al. 2006), where similar conclusions could be drawn. The injection model is supported by an independent study of Panaitescu et al. (2006).

3.4. Theoretical Implications

The following conclusions could be drawn from the above case studies:

1. A common feature of the early X-ray afterglow light curves is a well-defined temporal steepening break. A crucial observational fact is that there is essentially no spectral variation before and after the break. This suggests that the break is of hydrodynamic origin rather than due to the crossing of some typical frequencies of the synchrotron spectrum in the band. It is worth mentioning that a light-curve transition similar to the transition between segments II and III is expected in a radiative fireball (e.g., Böttcher & Dermer 2000; see, e.g., Figs. 1 and 2 of Wu et al. 2005). However, that transition is due to the crossing of ν_m in the observational band. One therefore expects a large spectral variation before and after the break, which is inconsistent with the data. Another straightforward interpretation would be a jet break, but there are three reasons against such an interpretation. First, in all of the cases, $p < 2$ has to be assumed. This is in stark contrast to the late jet breaks observed in the optical band, which typically have $p > 2$. Furthermore, the α - β relation predicted in the jet model is usually not satisfied. Second, the postbreak α - β relation is usually satisfied in a standard slow cooling ISM model, with the X-ray band either below or above the cooling frequency. In such a sense, this segment is quite normal. Third, in some cases (e.g., GRB 050315), another steepening break is observed after this normal segment, which is consistent with the jet break interpretation. Since only one break could be attributed to a jet break, the “shallow-to-normal” break must be due to something else.

2. A natural interpretation of the shallow decay phase is to attribute it to a continuous energy injection, so that the forward shock is “refreshed.” Three possibilities exist to account for the refreshed shock effect (§ 3.2): a long-lived central engine with progressively reduced activities, an instantaneous injection with a steep power-law distribution of the shell Lorentz factors, and the deceleration of an instantaneously injected highly magnetized (high σ) flow. In terms of afterglow properties, these possibilities are degenerate (e.g., the connection between q and s) and cannot be differentiated. In principle, the first scenario may give rise to additional observational signatures (e.g., Rees & Mészáros 2000; Gao & Wei 2004, 2005), which may be used to differentiate the model from the others.

3. Two interesting characteristics during the injection phase are that the injection process is rather smooth and that the effective q -value is around 0.5. This gives interesting constraints on the possible physical mechanisms. (1) For the scenario of a continuously injecting central engine (Zhang & Mészáros 2001),

the central engine luminosity must vary with time smoothly. This is in contrast to the conventional GRB central engine that injects energy erratically to allow the observed rapid variability in the light curves. This usually requires two different energy components, i.e., one “hot” fireball component that leads to the prompt emission and a “cold” Poynting flux component that gives to the smooth injection. A natural Poynting flux component is due to the spin-down of a newborn millisecond pulsar (Dai & Lu 1998a; Zhang & Mészáros 2001). However, a straightforward prediction from such a model is $q = 0$, not consistent with $q \sim 0.5$ inferred from the observations. Modifications to the simplest model are needed. Alternatively, the system may be a long-lived black hole torus system with a reducing accretion rate. However, at later times the long-term central engine power corresponds to $q = 5/3$ (MacFadyen et al. 2001; Janiuk et al. 2004), too steep to give an interesting injection signature. It is worth mentioning that in the collapsar simulations (MacFadyen et al. 2001), an extended flat injection episode sometimes lasts for ~ 1000 s, which could potentially interpret the short injection phase of some bursts, but it is difficult to account for some other bursts whose injection phase is much longer. (2) For the scenario of a power-law distribution of Lorentz factors (Rees & Mészáros 1998), one should require that a smooth distribution of Lorentz factors is produced after the internal shock phase. In the internal shock model, slow shells are indeed expected to follow the fast shells, but they tend to be discrete and give rise to bumpy light curves (e.g., Kumar & Piran 2000b) especially when the contribution from the reverse shock is taken into account (Zhang & Mészáros 2002a). It is also unclear how an effective $q \sim 0.5$ is expected. (3) Deceleration of a promptly ejected Poynting flux-dominated flow (e.g., Zhang & Kobayashi 2005) naturally gives a smooth injection signature observed. Above case studies indicate that the injected energy is by a factor of several to 10. Within such a picture, the unknown σ -value is about several to 10. However, it is unclear how long the delay would be and whether one can account for the shallow decay with $q \sim 0.5$ extending for 10^4 s. More detailed theoretical modeling is needed to test this hypothesis.

4. Any model needs to interpret the sudden cessation of the injection at t_{b2} . This time has different meanings within the three scenarios discussed above. (1) Within the long-lived central engine model, this is simply the epoch when the injection process ceases. In the pulsar injection model, there is a well-defined time for injection to become insignificant (Dai & Lu 1998a; Zhang & Mészáros 2001), but within a black hole torus injection model, such a time is not straightforwardly defined. (2) In the varying Lorentz factor scenario, this time corresponds to a cutoff of the Lorentz factor distribution at the low end below which the distribution index s is flatter than 1 so that they are energetically unimportant. This lowest Lorentz factor is defined by

$$\Gamma_m = 23 \left(\frac{E_{\text{iso},52}}{n} \right)^{1/8} t_{b2,4}^{-3/8} \left(\frac{1+z}{2} \right)^{3/8}. \quad (22)$$

A successful model must be able to address a well-defined Γ_m in this model. (3) Within the Poynting flux injection model, a well-defined time cutoff is expected, which corresponds to the epoch when all of the Poynting energy is transferred to the blast wave. If the shallow decay is indeed due to Poynting energy transfer, the cutoff time (t_{b2}) could be roughly defined by the σ parameter through $\sigma \sim (t_{b2}/t_{\text{dec}})^{(1-q)}$, where t_{dec} is the conventional deceleration time defined by $E_{\text{iso}}/(1+\sigma)$, when only a fraction of $(1+\sigma)^{-1}$ energy is transferred to the ISM (Zhang & Kobayashi 2005).

5. Although we have not tried hard to rule out a wind model interpretation, the case studies discussed above suggest that the early afterglow data are consistent with an ISM model for essentially all of the bursts. This conclusion also applies to other well-studied *Swift* bursts (e.g., GRB 050525a; Blustin et al. 2006). This result is intriguing given that long GRBs are associated with the death of massive stars, from which a strong wind is expected. Previous analyses using late-time afterglow data (e.g., Panaitescu & Kumar 2002; Yost et al. 2003) have also suggested that most afterglow data are consistent with an ISM model rather than a wind model. In order to accommodate the data, it has been suggested that the wind parameter may be small so that at a late enough time the blast wave is already propagating in an ISM (e.g., Chevalier et al. 2004). The *Swift* results push the ISM model to even earlier epochs (essentially right after the deceleration) and indicate the need for a reinvestigation of the problem. The epoch shortly before the deaths of massive stars is not well studied (Woosley et al. 2003). One possibility is that the stellar wind ceases some time before the star collapses. Careful analyses of early afterglows of a large sample of long GRBs may shed light on the final stage of massive star evolution.

4. REVERSE SHOCK EMISSION

4.1. Synchrotron Emission

It is generally believed that a short-lived reverse shock exists during the initial deceleration of the fireball and gives interesting emission signatures in the early afterglow phase. Given the same internal energy in both the forward-shocked and the reverse-shocked regions, the typical synchrotron frequency for the reverse shock emission is typically much lower than that in the forward shock region, since the ejecta is much denser than the medium. While the early forward shock synchrotron emission peaks in X-rays at early times, the reverse shock synchrotron emission usually peaks in the optical/IR band or even lower (e.g., Mészáros & Rees 1997a; Sari & Piran 1999; Kobayashi 2000; Zhang et al. 2003; Zhang & Kobayashi 2005). This model has been successful in interpreting the early optical emission from GRB 990123 (Akerlof et al. 1999; Sari & Piran 1999; Mészáros & Rees 1999), GRB 021211 (Fox et al. 2003; Li et al. 2003a; Wei 2003), and GRB 041219a (Blake et al. 2005; Vestrand et al. 2005; Fan et al. 2005c). As a result, it is expected that the reverse shock component has a negligible contribution in the X-ray band.

In the above argument, it has been assumed that the shock parameters (ϵ_e , ϵ_B , and p) are the same in both shocks. In reality this might not be the case. In particular, the GRB outflow may itself carry a dynamically important magnetic field component (or Poynting flux). This magnetic field would be shock compressed and amplified, giving a larger effective ϵ_B (Fan et al. 2004a, 2004b; Zhang & Kobayashi 2005). Since the medium is generally not magnetized, it is natural to expect different ϵ_B values in both regions, and a parameter $\mathcal{R}_B \equiv (\epsilon_{B,r}/\epsilon_{B,f})^2$ has been used in the reverse shock analysis. It has been found that \mathcal{R}_B is indeed larger than unity for GRB 990123 and GRB 021211 (Zhang et al. 2003; Fan et al. 2002; Kumar & Panaitescu 2003; Panaitescu & Kumar 2004; McMahon et al. 2004). Hereafter the subscripts/superscripts “*f*” and “*r*” represent the forward shock and the reverse shock, respectively. According to Zhang & Kobayashi (2005), the case of GRB 990123 corresponds to the most optimized case with $\sigma \sim 1$, so that \mathcal{R}_B is the largest.

More generally, ϵ_e and p may also vary in both shocks. Fan et al. (2002) performed a detailed fit to the GRB 990123 data and obtained $\epsilon_e^r = 4.7\epsilon_e^f$ and $\epsilon_B^r = 400\epsilon_B^f$. A general treatment therefore requires that we introduce one more parameter, i.e., $\mathcal{R}_e = [(p^r - 2)/(p^r - 1)]/[(p^f - 2)/(p^f - 1)](\epsilon_e^f/\epsilon_e^r)$. Following the

treatment of Zhang et al. (2003), we have the following relations in the thin-shell regime (see also Fan & Wei 2005):¹⁶

$$\frac{\nu_m^r(t_\times)}{\nu_m^f(t_\times)} \sim \mathcal{R}_B \mathcal{R}_e^2 \left(\frac{\gamma_{34,\times} - 1}{\Gamma_\times - 1} \right)^2, \quad (23)$$

$$\frac{\nu_c^r(t_\times)}{\nu_c^f(t_\times)} \sim \mathcal{R}_B^{-3} \left(\frac{1 + Y^f}{1 + Y^r} \right)^2, \quad (24)$$

$$\frac{F_{\nu,\max}^r(t_\times)}{F_{\nu,\max}^f(t_\times)} \sim \mathcal{R}_B \frac{\Gamma_\times^2}{\Gamma_0} \sim \mathcal{R}_B \Gamma_0, \quad (25)$$

where Y^f and Y^r are the Compton parameters for the forward and the reverse shock emission components, respectively; t_\times is the reverse shock crossing time, which is essentially t_{dec} (eq. [10]) for the thin-shell case; Γ_\times is the bulk Lorentz factor of the outflow at t_\times ; and $\gamma_{34,\times} \approx (\Gamma_0/\Gamma_\times + \Gamma_\times/\Gamma_0)/2$ is the Lorentz factor of the shocked ejecta relative to the unshocked one.

For typical parameters, both ν_m^f and ν_c^f are below the XRT band (comparing eqs. [7] and [8] with eq. [10]). According to equations (23) and (24), ν_c^r and ν_m^r should be also below the XRT band. Following the standard synchrotron emission model, we then derive the X-ray flux ratio of the reverse shock and the forward shock components at t_\times :

$$\frac{F_{\nu,X}^r(t_\times)}{F_{\nu,X}^f(t_\times)} \approx \mathcal{R}_B^{\frac{p-2}{2}} \mathcal{R}_e^{p-1} \Gamma_0 \left(\frac{\gamma_{34,\times} - 1}{\Gamma_\times - 1} \right)^{p-1} \left(\frac{1 + Y^f}{1 + Y^r} \right). \quad (26)$$

We can see that for $\mathcal{R}_B = \mathcal{R}_e = 1$, $Y^f = Y^r$, and $p \geq 2$, one has $F_{\nu,X}^r(t_\times) \leq F_{\nu,X}^f(t_\times)$, since $\gamma_{34,\times} \leq 1$ and $\Gamma_\times \sim \Gamma_0$ in the thin-shell case. The reverse shock contamination in the X-ray band is therefore not important. The situation changes if we allow higher \mathcal{R}_e and \mathcal{R}_B values. Increasing \mathcal{R}_e directly increases the reverse-to-forward flux ratio. Although the dependence on \mathcal{R}_B is only mild when p is close to 2, a higher \mathcal{R}_B suppresses the IC process in the reverse shock region relative to that in the forward shock region, so that the ratio $(1 + Y^f)/(1 + Y^r)$ also increases. As a result, as $\mathcal{R}_B \gg 1$ and $\mathcal{R}_e \gg 1$, the reverse shock synchrotron component would stick out above the forward shock synchrotron component, and an X-ray bump is likely to emerge (see also Fan & Wei 2005). As a numerical example, taking $p = 2.3$, $\Gamma_\times \approx \Gamma_0/2 = 50$, $\mathcal{R}_B = 10$, $\mathcal{R}_e = 5$, and $\epsilon_e^f = 30\epsilon_B^f$, we get $F_{\nu,X}^r(t_\times)/F_{\nu,X}^f(t_\times) \approx 6$. This could potentially explain the X-ray flare (by a factor of ~ 6) detected in GRB 050406 (Burrows et al. 2005a; P. Romano et al. 2006, in preparation). However, a big caveat of such a model is that one expects a very bright UV/optical flash due to the large \mathcal{R}_B and \mathcal{R}_e involved, like the case of GRB 990123. Unless this flash is completely suppressed by extinction, the nondetection of such a flash in the UVOT band for GRB 050406 strongly disfavors such an interpretation.

4.2. Synchrotron Self-Compton Emission

The synchrotron photons in the reverse shock region will be scattered by the same electrons that produce these photons. The characteristic energy of this component is typically in the gamma-

ray range. However, under some conditions, this synchrotron self-Compton (SSC) component would also stand out in the X-ray band, giving rise to an X-ray bump in the light curve. A detailed discussion has been presented in Kobayashi et al. (2005), which we do not repeat here. The general conclusion is that the SSC component could account for an early X-ray flare bump by a factor of several under certain optimized conditions. An advantage of this model over the reverse shock synchrotron model is that a bright UV–optical flash is avoided. However, this model cannot account for a flare with a very large contrast (e.g., by a factor of 500, as seen in GRB 050502B; Burrows et al. 2005a).

5. MECHANISMS TO PRODUCE EARLY X-RAY FLARES

XRT observations indicate that X-ray flares are common features in the early phase of X-ray afterglows (component V in Fig. 1). After the report of the first two cases of flares in GRB 050406 and GRB 050502B (Burrows et al. 2005a), later observations indicate that nearly half of long GRBs harbor early X-ray flares (e.g., O’Brien et al. 2006). More intriguingly, the early X-ray afterglow of the latest localized short GRB 050724 (Barthelmy et al. 2005b) also revealed flares similar to those in the long GRBs (e.g., GRB 050502B). The common feature of these flares is that the decay indices after the flares are typically very steep, with a $\delta t/t$ much smaller than unity. In some cases (e.g., GRB 050724; Barthelmy et al. 2005b), the postflare decay slopes are as steep as ≤ -7 . In this section we discuss various possible models to interpret the flares and conclude that the data require that the central engine is active and ejecting these episodic flares at later times.

5.1. Emission from the Reverse Shock?

As discussed in § 4, synchrotron or SSC emission from the reverse shock region could dominate that from the forward shock emission in the X-ray band under certain conditions. Because of the lack of strong UV–optical flares in the UVOT observations, we tentatively rule out the reverse shock synchrotron emission model. The prediction of the light curve in the SSC model could potentially interpret the X-ray flare seen in GRB 050406 (Burrows et al. 2005a), but the predicted amplitude is too low to interpret the case of GRB 050502B (Burrows et al. 2005a). In some bursts (e.g., GRB 050607), more than one flare is seen in a burst. Although one of these flares may be still interpreted as the reverse shock SSC emission, an elegant model should interpret these flares by a model with the same underlying physics. We tentatively conclude that the reverse shock model cannot account for most of the X-ray flares detected by the *Swift* XRT in a unified manner.

5.2. Density Clouds Surrounding the Progenitor?

Long-duration GRBs are believed to be associated with the deaths of massive stars, such as Wolf-Rayet stars. According to Woosley et al. (2003), there are no observations to constrain the mass-loss rate of a Wolf-Rayet star during the posthelium phase (100–1000 yr before the explosion). No stability analyses have been carried out to assess whether such stars are stable. At the high end of a reasonable range of the mass-loss rate, dense clouds surrounding a GRB progenitor may exist. For a wind velocity $v_w \sim 100 \text{ km s}^{-1}$, the density clumps could occur at a radius $\sim 3 \times 10^{16} - 3 \times 10^{17} \text{ cm}$. These density clumps have been invoked by Dermer & Mitman (1999, 2004) to interpret the GRB prompt emission variabilities.

One immediate question is whether these density clumps, if they exist, could give rise to the X-ray flares detected by XRT. In

¹⁶ For an arbitrary σ , the treatment becomes more complicated. The treatment presented here is generally valid for $\sigma \lesssim 1$. For $\sigma > 1$, the reverse shock emission starts to be suppressed (Zhang & Kobayashi 2005). Since we are investigating the most optimistic condition for the reverse shock contribution, in this paper we adopt the standard hydrodynamic treatment, which is valid for $\sigma \lesssim 1$.

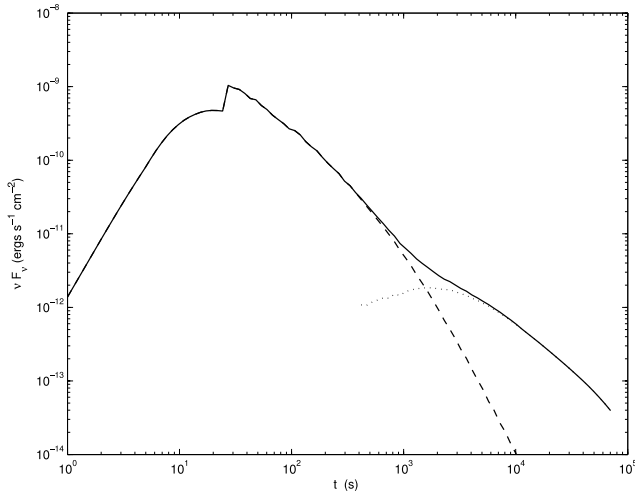


FIG. 4.—X-ray flare powered by a relativistic fireball interacting with a dense cloud. The cloud is located at $R = (3.0, 3.3) \times 10^{16}$ cm with a density $n_{\text{cloud}} = 100 \text{ cm}^{-3}$. The background ISM density is $n = 1 \text{ cm}^{-3}$. Other parameters include $E_{\text{iso}} = 10^{52}$ ergs, $z = 1$, $\Gamma_0 = 240$, $\epsilon_e = 0.1$, $\epsilon_B = 0.01$, $p = 2.3$, and $\theta_j = 0.1$. The dashed line is the X-ray emission contributed by the electrons shocked at $R < 3.3 \times 10^{16}$ cm, and the dotted line is the X-ray emission contributed by the electrons shocked at $R > 3.3 \times 10^{16}$ cm. The solid line is the sum of these two components.

order to check this possibility, we investigate the following toy model. For simplicity, we assume that a dense clump extends from $R \sim 3 \times 10^{16}$ cm to $(R + \Delta) \sim 3.3 \times 10^{16}$ cm with a number density $n_{\text{cloud}} \sim 100 \text{ cm}^{-3}$. The background ISM density is taken as $n \sim 1 \text{ cm}^{-3}$. Other parameters in the calculation include $E_{\text{iso}} = 10^{52}$ ergs, $z = 1$, $\Gamma_0 = 240$, $\epsilon_e = 0.1$, $\epsilon_B = 0.01$, $p = 2.3$, and $\theta_j = 0.1$. No sideways expansion of the jet is included, which is consistent with previous simulations (Kumar & Granot 2003; Cannizzo et al. 2004). The X-ray light curve is shown in Figure 4, the general feature of which is reproduced in both codes used in this paper. Although the rising phase could be very sharp, the decaying slope is rather flat. This is because of two effects. First, after entering the dense cloud, the blast wave Lorentz factor falls off rapidly. The observed time $t \sim R/2\Gamma^2$ is hence significantly stretched. The dashed line in Figure 4 represents the observed emission before the fireball exits the cloud. Second, after the fireball exits the cloud (dotted line in Fig. 4), the fireball does not decelerate immediately since the Lorentz factor is already too low to be further decelerated in a medium with a low density. It is decelerated again when enough medium is swept up at a larger radius. The interaction of a fireball with density bumps has been studied previously by many authors (e.g., Lazzati et al. 2002; Dai & Wu 2003). Our detailed calculations suggest that the variation caused by density inhomogeneities is generally not very significant (see also Ramirez-Ruiz et al. 2005). The light curves for a blast wave surfing on a density wave should be generally quite smooth (cf. Lazzati et al. 2002).

The one-dimensional model presented here effectively calculates the feature when the fireball encounters a high-density shell. A more realistic model for density clumps should include the size of the clump (Δ). The light-curve decay slope after the peak therefore depends on the comparison between Γ^{-1} and the angle the clump extends from the central engine, Δ/R . If $\Gamma^{-1} \ll \Delta/R$, the above calculation is still valid since the observer would not notice the edge of the clump. The resulting decay slope is rather shallow after the peak, which is in distinct contrast to the X-ray flare data. This is the case for the parameters we use in Figure 4. For smaller clumps, the light curve will steepen as Γ^{-1} becomes comparable

to Δ/R . Our numerical calculations indeed show such a feature. However, the flux does not fall rapidly right after the peak. The peak time is typically shortly after the blast wave enters the density clump when the Lorentz factor is still very high. The epoch when $\Gamma^{-1} = \Delta/R$ is satisfied happens much later. The light curve therefore still shows a shallow decay segment before the steep decay component. This is in contrast with the X-ray flare data that show rapid decays right after the flare peak (e.g., Burrows et al. 2005a; Falcone et al. 2006; Romano et al. 2006; O'Brien et al. 2006). One could make the clouds small enough, so that $\Gamma^{-1} > \Delta/R$ is satisfied from the very beginning. However, in such a case it is very hard to achieve a large contrast between the flares and the underlying afterglow level (Ioka et al. 2005). The factor of 500 time contrast observed in GRB 050502B is in any case very difficult to achieve within all of the density clump models we have explored. We therefore tentatively conclude that the X-ray flares commonly detected in the early X-ray afterglow light curves are likely not caused by the putative density clouds surrounding the GRB progenitors. The lack of these well-modeled features in the data also suggests that the lumpiness of the circumburst medium is, if any, rather mild. We note, however, that C. D. Dermer (2006, in preparation) suggests that more detailed three-dimensional modeling of the density clump problem may potentially reproduce the observed X-ray flares.

5.3. Two-Component Jet?

In the collapsar progenitor models, it is expected that the ejecta generally has two components, one ultrarelativistic component powering the GRB, and another moderately relativistic cocoon component (e.g., Zhang et al. 2004b; Mészáros & Rees 2001; Ramirez-Ruiz et al. 2002). This gives a physical motivation to the phenomenological two-component jet model (e.g., Lipunov et al. 2001; Berger et al. 2003; Huang et al. 2004). An interesting possibility would be whether the X-ray flare following the prompt gamma-ray emission (which arises from the central relativistic component) is caused by the deceleration of the wider mildly relativistic cocoon component as it interacts with the ambient medium. A straightforward conclusion is that the wide, off-beam component must contain more energy than the narrow component in order to give noticeable features in the light curve. Also the decay after the light-curve peak of the second component should follow the standard afterglow model, and the variability timescale satisfies $\delta t/t \sim 1$. The optical light curves of the two-component jet model have been calculated by Huang et al. (2004) and Granot (2005). Figure 5 shows a sample X-ray light curve in the two-component jet model. It is obvious that this model cannot interpret the rapid falloff observed in the XRT X-ray flares and is therefore ruled out.

5.4. Patchy Jets?

A related model considers a jet with large energy fluctuations in the angular direction, so that its energy distribution is patchy (Kumar & Piran 2000a). This is a variation of the two-component jet and could be approximated as a multicomponent jet. When the $1/\Gamma$ cone of different patches enters the field of view, the observed light curve may present interesting signatures. However, the general feature of the two-component jet still applies: only when a patch has a substantial energy compared with the on-beam jet would it give a bump feature on the light curve. After each bump, the afterglow level is boosted and would not resume the previous level. The variability timescale is also typically $\delta t/t \sim 1$. Figure 6 gives an example. Apparently this model cannot account for the observed X-ray flares.

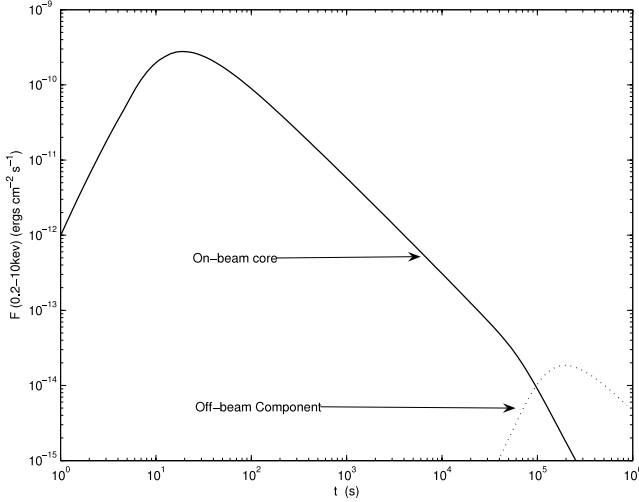


FIG. 5.—X-ray light curve powered by a two-component jet. The angular range $0 < \theta < 0.1$ is the central narrow component, which has $E_{\text{iso},n} = 10^{52}$ ergs and $\Gamma_{0,n} = 240$. The wide jet component covers a range of $0.1 < \theta < 0.3$, with $E_{\text{iso},w} = 5 \times 10^{52}$ ergs and $\Gamma_{0,w} = 50$. The ISM density is $n = 1 \text{ cm}^{-3}$. Other parameters include $\epsilon_e = 0.1$, $\epsilon_B = 0.01$, $p = 2.3$, and $z = 1$. The line of sight is at $\theta = 0$. The light-curve peak of the second component corresponds to the epoch when the off-beam wide component is decelerated, so that its $1/\Gamma_w$ beam enters the field of view.

5.5. Post Energy Injection into the Blast Wave?

In the internal shock model, it is expected that after the collisions are finished, the shells are distributed such that a shell with a higher Lorentz factor always leads a shell with a lower Lorentz factor. As the fast moving shell (blast wave) is decelerated, the trailing slow shell will catch up with it and inject energy into the blast wave (Kumar & Piran 2000b). Such an injection also happens if the central engine further ejects high- Γ shells that catch up with the decelerating blast wave (Zhang & Mészáros 2002a). Such a collision would give rise to a bump signature on the light curve. A detailed treatment suggests that the overall light curve should include emission from three components: a forward shock propagating into the medium, a second forward shock propagating into the blast wave, and a reverse shock propagating into the injected shell. In the X-ray band, the contribution from the reverse shock is negligible. The light curve generally shows a steplike signature, due to the increase of the total energy in the blast wave (Zhang & Mészáros 2002a). After the peak, the flux level does not resume the previous level since more energy has been injected into the fireball. The decay slope after the injection peak follows the standard afterglow model, and $\delta t/t \sim 1$ is expected. These are also inconsistent with the data of X-ray flares.

5.6. Neutron Signature?

Another interesting possibility is whether X-ray flashes are the signature of the existence of free neutrons in the fireball. Derishev et al. (1999), Beloborodov (2003), and Rossi et al. (2004) suggested that a baryonic fireball contains free neutrons, the decay of which would leave important imprints on the light curve. Fan et al. (2005b) modeled the process carefully and calculated the light curves. According to Fan et al. (2005b), the neutron feature is rather smooth in a wind model, and it is hard to detect. In the ISM case, on the other hand, a bump does exist (in all bands). The physical reason is that the trailing proton shell catches up with the decelerated neutron decay products. The physical process is analogous to the post energy injection effect discussed in § 5.5. The amplitude of the flare is modest, at most a factor of several.

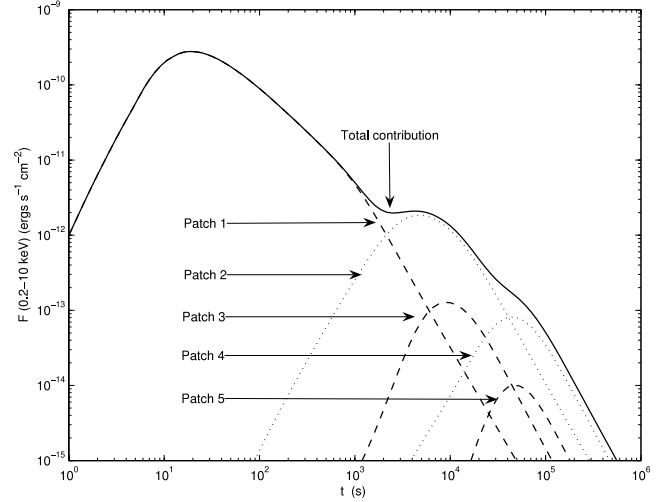


FIG. 6.—X-ray light curve powered by a patchy jet. For simplicity, an annular patchy jet is simulated. The following parameters are adopted: $0 < \theta < 0.02$, $E_{\text{iso},1} = 10^{52}$ ergs, $\Gamma_{0,1} = 240$ for patch 1 (the on-beam jet); $0.02 < \theta < 0.04$, $E_{\text{iso},2} = 5 \times 10^{52}$ ergs, $\Gamma_{0,2} = 50$ for patch 2; $0.04 < \theta < 0.06$, $E_{\text{iso},3} = 10^{52}$ ergs, $\Gamma_{0,3} = 240$ for patch 3; $0.06 < \theta < 0.08$, $E_{\text{iso},4} = 5 \times 10^{52}$ ergs, $\Gamma_{0,4} = 50$ for patch 4; $0.08 < \theta < 0.10$, $E_{\text{iso},5} = 10^{52}$ ergs, $\Gamma_{0,5} = 240$ for patch 5. Other parameters are the same as in Fig. 5.

Since the injection model is not favored, this possibility is also disfavored.

5.7. Late Central Engine Activity

After ruling out various “external origin” mechanisms, we are left only with the possibility that involves the reactivation of the central engine. In this interpretation, the X-ray flares share essentially the same origin as the prompt gamma-ray emission; i.e., they are caused by some “internal” energy dissipation processes that occur before the ejecta is decelerated by the ambient medium. The leading scenario is the “late” internal shock model, which suggests that the central engine ejects more energy in the form of an unsteady wind with varying Lorentz factors at a late time. These discrete shells collide with each other and produce the observed emission. Alternatively, the late injection could be mainly in the form of magnetic fields/Poynting flux, and the X-ray flares are due to the intermittent dissipation of the magnetic fields, likely through magnetic reconnection events. Fan et al. (2005a) argued that at least for the flares following short GRBs, the process that powers the flares has to be of magnetic origin.

There are two advantages of the internal models over the external models:

1. First, restarting the central engine equivalently resets the time zero point. In this interpretation, the observed flare component and the underlying decaying component observed at the same observer time t originate from different physical sites at different central engine times. Let us assume that the initial burst lasts T_{90} , that the central engine reactivates after a time interval Δt , and that it ejects an unsteady wind with a typical variability timescale of δt . At the observer time $t = T_{90} + \Delta t \sim 1000$ s, the underlying decaying component (external afterglow) happens at a distance $R_{\text{ex}} \sim [\Gamma(t)]^2 ct \sim 5 \times 10^{16}$ cm, where $\Gamma(t)$ is the Lorentz factor of the blast wave at the time t . The flare, on the other hand, happens at a distance of $R_{\text{in}} \sim \Gamma_0^2 c \delta t \sim (10^{13} - 10^{14})$ cm, where Γ_0 is the initial Lorentz factor of the late-time ejecta. According to the clocks attached to the central engine, the photons from the external afterglow component are emitted at $\hat{t}_{\text{ex}} \sim R_{\text{ex}}/c \sim 1.7 \times 10^6$ s, while the photons from late central engine activity are emitted at

$\hat{t}_{\text{in}} \sim t + R_{\text{in}}/c \sim 10^3 + R_{\text{in}}/c \sim 10^3 - 10^4$ s. Because of the relativistic effect, these photons reach the observer at exactly the same time t and superpose onto the light curve detected by the observer. When plotted as a single log-log light curve with the origin at the burst trigger, a very steep apparent decay slope can be produced for a large time shift Δt (Fig. 3). This naturally overcomes the $\delta t/t \geq 1$ constraint encountered by the external models (Ioka et al. 2005 and references therein).

2. Second, invoking a late central engine activity greatly eases the required energy budget. In most of the external models, in order to give rise to a significant bump on the light curve, the total newly added energy (either from the radial direction—late injection case or from the horizontal direction—patchy jets or multiple-component jets) must be at least comparable to the energy that defines the afterglow emission level. This model therefore demands a very large energy budget. For the internal model, on the other hand, since the light curve is a superposition of two independent physical components, the energy budget is greatly reduced, especially if the bump happens at later times when the background afterglow level is much lower. For example, for an X-ray light curve with the decay index of -1 following a burst with duration 10 s, a significant flare at $\sim 10^4$ s only requires a luminosity slightly larger than 10^{-3} times that of the prompt emission. This model is therefore very “economical” in interpreting the very late ($>10^4$ s) flares detected in some bursts (e.g., GRB 050502B, Falcone et al. 2006; GRB 050724, Barthelmy et al. 2005b).

Can late central engine activity give rise to softer bursts (e.g., X-ray flares as compared with the prompt gamma-ray or hard X-ray emission)? According to the internal shock model, the peak energy E_p of the synchrotron spectrum satisfies (Zhang & Mészáros 2002c)

$$E_p \propto \Gamma B' \propto L^{1/2} r^{-1} \propto L^{1/2} \Gamma^{-2} \delta t^{-1}, \quad (27)$$

where L is the luminosity, $B' \propto (L/\Gamma^2 r^2)^{1/2}$ is the comoving magnetic field strength, Γ is the typical Lorentz factor of the ejecta (for internal shock collisions, this Γ is for slow shells), and δt is the variability timescale. We can see that a smaller L , a higher Γ , and a larger δt would be favorable for a softer burst. The observed XRT X-ray flares generally have a smaller luminosity L . The light curve is smoother with a larger δt (Burrows et al. 2005a; Barthelmy et al. 2005b). Also, at later times, the environment tends to be cleaner so that Γ could be larger. One therefore naturally expects softer flares at later times.

Can the central engine restart after being quiescent for some time (e.g., $\sim 10^3$ s, but sometimes as late as $\sim 10^5$ s)? This is an interesting theoretical problem. The collapsar model predicts a central engine timescale of minutes to hours (MacFadyen et al. 2001). The star may fragment into several pieces during the collapse (King et al. 2005). The largest piece collapses first onto the black hole, powering a prompt gamma-ray burst. Other fragments are initially ejected into elliptical orbits but would eventually fall into the black hole after some time, powering the late X-ray flares. Fragmentation could also happen within the accretion disk itself due to gravitational instabilities (Perna et al. 2006). A magnetic-dominated accretion flow could also give rise to intermittent accretion flows due to interplay between the gravity and the magnetic barrier (Proga & Begelman 2003; Proga & Zhang 2006). Flares could also occur if the central engine is a differentially rotating neutron star rather than a black hole (Dai et al. 2006). The rich information collected by the *Swift* XRT suggests that we are getting closer to unraveling the details of the bursting

mechanisms of GRBs. More detailed studies are called for to unveil the mystery of these explosions.

An interesting fact (see next subsection for case studies) is that the duration of the flares is positively correlated with the time at which the flare occurs. The later the flare, the longer the flare duration. A successful central engine model must be able to address such a peculiar behavior. Perna et al. (2006) suggest that if the accretion disk is fragmented into blobs or otherwise has large-amplitude density fluctuation at large radii from the central engine, the viscous disk evolution would cause more spread for blobs farther out from the central engine. This gives a natural mechanism for the observed correlation. Perna et al. (2006) suggest that gravitational instability in the outer part of the disk is likely the origin of the density inhomogeneity within the disk.

5.8. Case Studies

In this subsection we briefly discuss the X-ray flares discovered in several GRBs.

GRB 050406 and GRB 050502B (Burrows et al. 2005a).—These were the first two bursts with flares detected by XRT. For the case of GRB 050406, whose T_{90} is ~ 5 s, an X-ray flare starts at ~ 150 s and reaches a peak at ~ 230 s. The flux rebrightening at the flare peak is by a factor of 6. The rising and the decaying indices are ~ 4.9 and ~ -5.7 , respectively. The total energy emitted during the flare is about 10% of that emitted in the prompt emission. This suggests that the central engine becomes active again after ~ 150 s, but with a reduced power. For the case of GRB 050502B, whose T_{90} is ~ 17.5 s, a giant flare starts at ~ 300 s and reaches a peak at ~ 740 s. The flux rebrightening is by a factor of ~ 500 . The decay index after the peak is approximately -6 . The total energy emitted during the flare is comparable to that emitted in the prompt emission. This suggests that the central engine restarts and ejects a substantial amount of energy. The duration of the X-ray flare is much longer than the duration of the prompt emission (T_{90}), so that the luminosity of the flare is much lower. In GRB 050502B, there is yet another late flarelike event that peaks at $\sim 7 \times 10^4$ s. The postpeak decay index is approximately -3 . This is also consistent with the case of a late-time central engine activity, and the decaying slope is consistent with that expected from the curvature effect. The total energy emitted in this flare is $\sim 10\%$ of that emitted in the giant flare at ~ 740 s.

GRB 050724 (Barthelmy et al. 2005b).—This is a short, hard burst with $T_{90} \sim 3$ s whose host galaxy is an elliptical galaxy, similar to the case of the first *Swift*-localized short burst GRB 050509B (Gehrels et al. 2005). The XRT light curve reveals rich features that are quite similar to the case of GRB 050502B. The XRT observation starts at ~ 74 s after the trigger, and the early XRT light curve initially shows a steep decay with a slope of approximately -2 . This component is connected to the extrapolated BAT light curve that shows a flarelike event around 60–80 s. This extended flarelike epoch (including the -2 decay component) stops at ~ 200 s, after which the light curve decays even more rapidly (with an index less than -7). A second, less energetic flare peaks at ~ 300 s, which is followed by another steep (with index less than -7) decay. A third, significant flare starts at $\sim 2 \times 10^4$ s, and the decay index after the peak is approximately -2.8 . This is quite similar to the late flare seen in GRB 050502B. The energy emitted during the third flare is comparable to that of the second one, and both are several times smaller than the energy of the first flare. All of the rapid-decay components following the flares could be potentially interpreted as the high-latitude emission, given a proper shift of the zero time point. Since the duration of the third flare is very long, the t_0 effect does not affect the decay index too

much. This is why the decay index -2.8 is quite normal, i.e., consistent with the $-2 - \beta$ prediction. The earlier steeper decays (e.g., less than -7) are all preceded by flares with a sharp increasing phase. Shifting t_0 in these cases would lead to significant flattening of the decaying index, which could be still consistent with the high-latitude emission. All of these discussions also apply to the case of GRB 050502B.¹⁷

GRB 011121 (Piro et al. 2005).—This *BeppoSAX* burst also indicated a flarelike event around ~ 270 s. Piro et al. (2005) interpreted the X-ray bump as the onset of the afterglow phase. In view of the fact that X-ray flares are commonly detected in *Swift* bursts, it is natural to speculate that the event is also an X-ray flare caused by late central engine activity. Fan & Wei (2005) have suggested the late central engine activity and performed a detailed case study on this event.

6. CONCLUSIONS

During the past several months, the *Swift* XRT has collected a rich sample of early X-ray afterglow data. This, for the first time, allows us to peer at the final temporal gap left by the previous observations and to explore many interesting questions of GRB physics. In this paper we have systematically investigated various possible physical processes that could give interesting contributions to the early X-ray afterglow observations. This includes the tail emission of the prompt gamma-ray emission, both the forward shock and the reverse shock emission components, refreshed shocks, post energy injection, medium-density clumps near the burst, angular inhomogeneities of the fireball, an emission component due to the presence of free neutrons, and emission from late central engine activity. We discuss how the above processes might leave interesting signatures on the early X-ray afterglow light curves.

Based on the XRT data collected so far, we summarize the salient features and suggest a tentative synthetic light curve for the X-ray afterglow light curves. As shown in Figure 1, the synthetic light curve includes five components: (I) an initial steep decay component; (II) a shallower than normal decay component; (III) a “normal” decay component; (IV) a post-jet break component; and (V) X-ray flares. Components I and III appear in almost all of the bursts. The other three components also commonly appear in some bursts. Flares have been detected in nearly half of the XRT early light curves, and the shallow decay segment has also been discovered in a good fraction of *Swift* GRBs. We therefore believe that they represent some common underlying physics for GRBs. After comparing data with various physical models, we tentatively draw the following conclusions:

1. The rapid decay component (Tagliaferri et al. 2005) commonly observed in the very early afterglow phase (which usually has a different spectral slope than the late shallow decay components) is very likely the tail emission of the prompt gamma-ray bursts or of the early X-ray flares. Allowing proper shifting of the time zero point and considering the contribution of the underlying forward shock emission, we speculate that essentially all of the steep decay cases could be understood in terms of the “curvature effect” of the high-latitude emission as the emission ceases abruptly. More detailed data analyses (Liang et al. 2006) support such a speculation.

2. The transition between the prompt emission and the afterglow emission appears to be universally represented by a rapid decay followed by a shallower decay, indicating that the GRB

emission site is very likely different from the afterglow site and that the apparent gamma-ray efficiency is very high.

3. In a good fraction of GRBs (e.g., GRB 050128, GRB 050315, GRB 050319, GRB 050401; Campana et al. 2005; Vaughan et al. 2006; Cusumano et al. 2006; De Pasquale et al. 2006), a clear temporal break exists in the early X-ray light curves. There is no obvious spectral index change across the break. The temporal decay index before the break is very flat, while that after the break is quite normal, i.e., is consistent with the standard afterglow model for a fireball with constant energy expanding into an ISM. We suggest that these breaks are likely not “jet breaks.” Rather, they mark the cessation of an early continuous energy injection phase during which the external shock is refreshed. We suggest three possible physical mechanisms for the refreshed shocks, i.e., a long-lived central engine with a decaying luminosity, a power-law distribution of the shell Lorentz factors before deceleration begins, and the deceleration of a high- σ flow. Further studies are needed to better understand this phase.

4. In the normal phase, the data for many bursts are consistent with an ISM rather than a wind medium. This has important implications for understanding the massive star progenitors of long GRBs, including their late evolution stage shortly before explosion.

5. Given that most of the shallow-to-normal transitions are due to the cessation of the refreshed shock phase, the cases with a well-identified jet break are not very common. Nonetheless, jet breaks are likely identified in some bursts, e.g., GRB 050315 (Vaughan et al. 2006), GRB 050525A (Blustin et al. 2006), XRF 050416 (Sakamoto et al. 2006), and some others.

6. The X-ray flares detected in nearly half of the *Swift* bursts are most likely due to late central engine activity, which results in internal shocks (or similar energy dissipation events) at later times. It seems to us that there is no evidence for the existence of density clumps in the GRB neighborhood, and there is no support for strong angular inhomogeneities (e.g., two-component jet, patchy jets) for the GRB fireball. However, their existence is not ruled out.

7. The similar light curves for some long GRBs (e.g., GRB 050502B; Burrows et al. 2005a) and some short GRBs (e.g., GRB 050724; Barthelmy et al. 2005b) indicate that different progenitor systems may share some similarities in the central engine. This might be caused by the same underlying physics that controls the hyperaccreting accretion disk, a common agent in charge of both types of systems (Perna et al. 2006).

The *Swift* XRT is still rapidly accumulating data on the early X-ray afterglows. More careful statistical analyses of these X-ray data, as well as more detailed case studies, also including low-frequency data collected by UVOT and other ground-based telescopes, would greatly improve our knowledge about GRB prompt emission and afterglows, advancing the quest for the final answers to the core questions in the study of GRBs.

We thank the referee for helpful comments. B. Z. acknowledges useful discussions with T. Abel, P. Armitage, M. Begelman, Z. G. Dai, C. D. Dermer, B. Dingus, C. Fryer, L. J. Gou, J. Granot, A. Heger, D. Lazzati, A. Panaitescu, R. Perna, D. Proga, S. Woosley, X. Y. Wang, X. F. Wu, and W. Zhang on various topics covered in this paper. This work is supported by NASA NNG05GB67G, NNG05GH91G (for B. Z.), NNG05GH92G (for B. Z., S. K., and P. M.), Eberly Research Funds of Penn State, and by the Center for Gravitational Wave Physics under grants PHY-01-14375 (for S. K.), NSF AST 0307376 and NASA NAG5-13286 (for P. M.), and NASA NAS5-00136 (D. B. and J. N.).

¹⁷ After submitting this paper, detailed data analyses (Liang et al. 2006) confirm these speculations. The late flares in both GRB 050724 and GRB 050502B are consistent with the hypothesis that they are due to late-time central engine activity.

REFERENCES

- Akerlof, C., et al. 1999, *Nature*, 398, 400
- Band, D., et al. 1993, *ApJ*, 413, 281
- Baring, M. G., & Harding, A. K. 1997, *ApJ*, 491, 663
- Barthelmy, S., et al. 2005a, *ApJ*, 635, L133
- . 2005b, *Nature*, 438, 994
- Beloborodov, A. M. 2000, *ApJ*, 539, L25
- . 2003, *ApJ*, 585, L19
- Berger, E., Cenko, S. B., & Kulkarni, S. 2005, *GCN Circ.* 3088, <http://gcn.gsfc.nasa.gov/gcn/gcn3/3088.gcn3>
- Berger, E., et al. 2003, *Nature*, 426, 154
- Blake, C. H., et al. 2005, *Nature*, 435, 181
- Blustin, A. J., et al. 2006, *ApJ*, 637, 901
- Böttcher, M., & Dermer, C. D. 2000, *ApJ*, 532, 281
- Burenin, R. A., et al. 1999, *A&A*, 344, L53
- Burrows, D. N., et al. 2005a, *Science*, 309, 1833
- . 2005b, *Space Sci. Rev.*, 120, 165
- Campana, S., et al. 2005, *ApJ*, 625, L23
- Cannizzo, J. K., Gehrels, N., & Vishniac, E. T. 2004, *ApJ*, 601, 380
- Chevalier, R. A., & Li, Z.-Y. 2000, *ApJ*, 536, 195
- Chevalier, R. A., Li, Z.-Y., & Fransson, C. 2004, *ApJ*, 606, 369
- Chincarini, G., et al. 2005, *ApJ*, submitted (astro-ph/0506453)
- Cusumano, G., et al. 2006, *ApJ*, 639, 316
- Dai, Z. G. 2004, *ApJ*, 606, 1000
- Dai, Z. G., & Cheng, K. S. 2001, *ApJ*, 558, L109
- Dai, Z. G., & Lu, T. 1998a, *A&A*, 333, L87
- . 1998b, *MNRAS*, 298, 87
- Dai, Z. G., Wang, X. Y., Wu, X. F., & Zhang, B. 2006, *Science*, 311, 1127
- Dai, Z. G., & Wu, X. F. 2003, *ApJ*, 591, L21
- Daigne, F., & Mochkovitch, R. 1998, *MNRAS*, 296, 275
- De Pasquale, M., et al. 2006, *MNRAS*, 365, 1031
- Derishev, E. V., Kocharovskiy, V. V., & Kocharovskiy, V. V. 1999, *ApJ*, 521, 640
- Dermer, C. 2004, *ApJ*, 614, 284
- Dermer, C., & Mitman, K. E. 1999, *ApJ*, 513, L5
- . 2004, in *ASP Conf. Ser.* 312, *Third Rome Workshop on Gamma-Ray Bursts in the Afterglow Era*, ed. M. Feroci et al. (San Francisco: ASP), 301
- Drenkhahn, G., & Spruit, H. C. 2002, *A&A*, 391, 1141
- Dyks, J., Zhang, B., & Fan, Y. Z. 2005, *ApJ*, submitted (astro-ph/0511699)
- Falcone, A., et al. 2006, *ApJ*, 641, 1010
- Fan, Y. Z., Dai, Z. G., Huang, Y. F., & Lu, T. 2002, *Chinese J. Astron. Astrophys.*, 2, 449
- Fan, Y. Z., & Wei, D. M. 2005, *MNRAS*, 364, L42
- Fan, Y. Z., Wei, D. M., & Wang, C. F. 2004a, *A&A*, 424, 477
- Fan, Y. Z., Wei, D. M., & Zhang, B. 2004b, *MNRAS*, 354, 1031
- Fan, Y. Z., Zhang, B., & Proga, D. 2005a, *ApJ*, 635, L129
- Fan, Y. Z., Zhang, B., & Wei, D. M. 2005b, *ApJ*, 628, 298
- . 2005c, *ApJ*, 628, L25
- Fenimore, E. E., Madras, C. D., & Nayakshin, S. 1996, *ApJ*, 473, 998
- Fox, D., et al. 2003, *ApJ*, 586, L5
- Freedman, D. L., & Waxman, E. 2001, *ApJ*, 547, 922
- Fynbo, J. P. U., Hjorth, J., Jensen, B. L., Jakobsson, P., Møller, P., & Naranen, J. 2005a, *GCN Circ.* 3136, <http://gcn.gsfc.nasa.gov/gcn/gcn3/3136.gcn3>
- Fynbo, J. P. U., et al. 2005b, *GCN Circ.* 3176, <http://gcn.gsfc.nasa.gov/gcn/gcn3/3176.gcn3>
- Gao, W. H., & Wei, D. M. 2004, *ApJ*, 604, 312
- . 2005, *ApJ*, 628, 853
- Gehrels, N., et al. 2005, *Nature*, 437, 851
- Giblin, T. W., et al. 1999, *ApJ*, 524, L47
- Goad, M. 2006, *A&A*, in press (astro-ph/0511751)
- Gou, L. J., Dai, Z. G., Huang, Y. F., & Lu, T. 2001, *A&A*, 368, 464
- Granot, J. 2005, *ApJ*, 631, 1022
- Granot, J., & Kumar, P. 2003, *ApJ*, 591, 1086
- Hill, J., et al. 2006, *ApJ*, 639, 303
- Huang, Y. F., Gou, L. J., Dai, Z. G., & Lu, T. 2000, *ApJ*, 543, 90
- Huang, Y. F., Wu, X. F., Dai, Z. G., Ma, H. T., & Lu, T. 2004, *ApJ*, 605, 300
- Ioka, K., Kobayashi, S., & Zhang, B. 2005, *ApJ*, 631, 429
- Janiuk, A., Perna, R., Di Matteo, T., & Czerny, B. 2004, *MNRAS*, 355, 950
- Kelson, D., & Berger, E. 2005, *GCN Circ.* 3100, <http://gcn.gsfc.nasa.gov/gcn/gcn3/3100.gcn3>
- King, A., O'Brien, P. T., Goad, M. R., Osborne, J., Olsson, E., & Page, K. 2005, *ApJ*, 630, L113
- Kobayashi, S. 2000, *ApJ*, 545, 807
- Kobayashi, S., Piran, T., & Sari, R. 1997, *ApJ*, 490, 92
- Kobayashi, S., & Sari, R. 2001, *ApJ*, 551, 934
- Kobayashi, S., & Zhang, B. 2003a, *ApJ*, 582, L75
- . 2003b, *ApJ*, 597, 455
- Kobayashi, S., Zhang, B., Mészáros, P., & Burrows, D. N. 2005, *ApJ*, submitted (astro-ph/0506157)
- Kumar, P. 1999, *ApJ*, 523, L113
- Kumar, P., & Granot, J. 2003, *ApJ*, 591, 1075
- Kumar, P., & Panaitescu, A. 2000a, *ApJ*, 541, L9
- . 2000b, *ApJ*, 541, L51
- . 2003, *MNRAS*, 346, 905
- Kumar, P., & Piran, T. 2000a, *ApJ*, 532, 286
- . 2000b, *ApJ*, 535, 152
- Lazzati, D., et al. 2002, *A&A*, 396, L5
- Li, W. D., Filippenko, A. V., Chornock, R., & Jha, S. 2003a, *ApJ*, 586, L9
- Li, Z., Dai, Z. G., Lu, T., & Song, L. M. 2003b, *ApJ*, 599, 380
- Liang, E. W., et al. 2006, *ApJ*, submitted (astro-ph/0602142)
- Lipunov, V. M., Postnov, K. A., & Prokhorov, M. E. 2001, *Astron. Rep.*, 45, 236
- Lithwick, Y., & Sari, R. 2001, *ApJ*, 555, 540
- Lloyd-Ronning, N. M., & Zhang, B. 2004, *ApJ*, 613, 477
- Lyutikov, M., & Blandford, R. D. 2003, *MNRAS*, submitted (astro-ph/0312347)
- MacFadyen, A. I., Woosley, S. E., & Heger, A. 2001, *ApJ*, 550, 410
- Mason, K. O., et al. 2006, *ApJ*, 639, 311
- McMahon, E., Kumar, P., & Panaitescu, A. 2004, *MNRAS*, 354, 915
- Mészáros, P., & Rees, M. J. 1993, *ApJ*, 405, 278
- . 1997a, *ApJ*, 476, 232
- . 1997b, *ApJ*, 482, L29
- . 1999, *MNRAS*, 306, L39
- . 2001, *ApJ*, 556, L37
- Moderski, R., Sikora, M., & Bulik, T. 2000, *ApJ*, 529, 151
- Nakar, E., & Piran, T. 2004, *MNRAS*, 353, 647
- Nousek, J., et al. 2006, *ApJ*, 642, 389
- O'Brien, P., et al. 2006, *ApJ*, submitted (astro-ph/0601125)
- Paczynski, B., & Xu, G. 1994, *ApJ*, 427, 708
- Panaitescu, A., & Kumar, P. 2002, *ApJ*, 571, 779
- . 2004, *MNRAS*, 353, 511
- Panaitescu, A., & Mészáros, P. 1999, *ApJ*, 526, 707
- Panaitescu, A., Mészáros, P., Gehrels, N., Burrows, D., & Nousek, J. 2006, *MNRAS*, in press (astro-ph/0508340)
- Panaitescu, A., Mészáros, P., & Rees, M. J. 1998, *ApJ*, 503, 314
- Panaitescu, A., Spada, M., & Mészáros, P. 1999, *ApJ*, 522, L105
- Perna, R., Armitage, P. J., & Zhang, B. 2006, *ApJ*, 636, L29
- Piro, L., et al. 1998, *A&A*, 331, L41
- . 2005, *ApJ*, 623, 314
- Proga, D., & Begelman, M. 2003, *ApJ*, 592, 767
- Proga, D., & Zhang, B. 2006, *ApJ*, submitted (astro-ph/0601272)
- Ramirez-Ruiz, E., Celotti, A., & Rees, M. J. 2002, *MNRAS*, 337, 1349
- Ramirez-Ruiz, E., Garcia-Segura, G., Salmonson, J. D., & Perez-Rendon, B. 2005, *ApJ*, 631, 435
- Rees, M. J., & Mészáros, P. 1992, *MNRAS*, 258, 41P
- . 1994, *ApJ*, 430, L93
- . 1998, *ApJ*, 496, L1
- . 2000, *ApJ*, 545, L73
- . 2005, *ApJ*, 628, 847
- Rhoads, J. E. 1999, *ApJ*, 525, 737
- Romano, P., et al. 2006, *A&A*, submitted (astro-ph/0602497)
- Rossi, E., Beloborodov, A. M., & Rees, M. J. 2004, in *AIP Conf. Proc.* 727, *Gamma-Ray Bursts: 30 Years of Discovery*, ed. E. E. Fenimore & M. Galassi (New York: AIP), 198
- Rossi, E., Lazzati, D., & Rees, M. J. 2002, *MNRAS*, 332, 945
- Sakamoto, T., et al. 2006, *ApJ*, 636, L73
- Salmonson, J. D. 2003, *ApJ*, 592, 1002
- Sari, R., & Mészáros, P. 2000, *ApJ*, 535, L33
- Sari, R., & Piran, T. 1997, *ApJ*, 485, 270
- . 1999, *ApJ*, 517, L109
- Sari, R., Piran, T., & Halpern, J. P. 1999, *ApJ*, 519, L17
- Sari, P., Piran, T., & Narayan, R. 1998, *ApJ*, 497, L17
- Tagliaferri, G., et al. 2005, *Nature*, 436, 985
- Thompson, C. 1994, *MNRAS*, 270, 480
- Usov, V. V. 1992, *Nature*, 357, 472
- Vaughan, S., et al. 2006, *ApJ*, 638, 920
- Vestrand, W. T., et al. 2005, *Nature*, 435, 178
- Wang, X. Y., Dai, Z. G., & Lu, T. 2000, *MNRAS*, 319, 1159
- Waxman, E., Kulkarni, S. R., & Frail, D. 1998, *ApJ*, 497, 288
- Wei, D. M. 2003, *A&A*, 402, L9
- Woosley, S. E., Zhang, W., & Heger, A. 2003, in *AIP Conf. Proc.* 662, *Gamma-Ray Burst and Afterglow Astronomy 2001*, ed. G. R. Ricker & R. K. Vanderspek (New York: AIP), 185

- Wu, X. F., Dai, Z. G., Huang, Y. F., & Lu, T. 2003, MNRAS, 342, 1131
———. 2005, ApJ, 619, 968
Yamazaki, R., Ioka, K., & Nakamura, T. 2004, ApJ, 607, L103
Yost, S., Harrison, F. A., Sari, R., & Frail, D. A. 2003, ApJ, 597, 459
Zhang, B., Dai, X., Lloyd-Ronning, N. M., & Mészáros, P. 2004a, ApJ, 601, L119
Zhang, B., & Kobayashi, S. 2005, ApJ, 628, 315
Zhang, B., Kobayashi, S., & Mészáros, P. 2003, ApJ, 595, 950
Zhang, B., & Mészáros, P. 2001, ApJ, 552, L35
———. 2002a, ApJ, 566, 712
———. 2002b, ApJ, 571, 876
———. 2002c, ApJ, 581, 1236
———. 2004, Int. J. Mod. Phys. A, 19, 2385
Zhang, W., Woosley, S. E., & Heger, A. 2004b, ApJ, 608, 365